MGD Application to a Blunt Body in Two-Dimensions

EDISSON SÁVIO DE GÓES MACIEL

IEA – Aeronautical Engineering Division

ITA – Aeronautical Technological Institute

Praça Mal. Eduardo Gomes, 50 – Vila das Acácias – São José dos Campos – SP – 12228-900

BRAZIL

edissonsavio@yahoo.com.br

Abstract: - In this paper, the Euler and Navier-Stokes equations are solved, according to a finite volume formulation and symmetrical structured discretization, applied to the problem of a blunt body in two-dimensions. The work of Gaitonde is the reference one to present the fluid dynamics and Maxwell equations of electromagnetism based on a conservative and finite volume formalisms. The MacCormack and the Jameson and Mavriplis symmetrical schemes are applied to solve the conserved equations. Two types of numerical dissipation models are applied, namely: Mavriplis and Azevedo. A spatially variable time step procedure is employed aiming to accelerate the convergence of the numerical schemes to the steady state solution. The results have proved that, when the Jameson and Mavriplis scheme is employed, an increase in the shock standoff distance is observed, which guarantees a minor increase in the temperature at the blunt body nose, and a minor increase in the drag aerodynamic coefficient.

Key-Words: Euler and Navier-Stokes equations, Magnetogasdynamics formulation, MacCormack algorithm, Jameson and Mavriplis algorithm, Finite volumes, Two-dimensional space.

1 Introduction

The effects associated with the interaction of magnetic forces with conducting fluid flows have been profitably employed in several applications related to nuclear and other ([1]) technologies and are known to be essential in the explanation of astrophysical phenomena. In recent years, however, the study of these interactions has received fresh impetus in the effort to solve the problems of high drag and thermal loads encountered in hypersonic flight. The knowledge that electrical and magnetic forces can have profound influence on hypersonic flowfields is not new ([2] and [3]) – note increased shock-standoff and reduced heat transfer rates in hypersonic flows past blunt bodies under the application of appropriate magnetic fields. The recent interest stems, however, from new revelations of a Russian concept vehicle, known as the AJAX ([4]), which made extensive reference to technologies requiring tight coupling between electromagnetic and fluid dynamic phenomena. A magnetogasdynamics (MGD) generator was proposed ([5]) to extract energy from the incoming air while simultaneously providing more benign flow to the combustion components downstream. The extracted energy could then be employed to increase thrust by MGD pumping of the flow exiting the nozzle or to assist in the generation of a plasma for injection of the body. This latter technique is known to not only reduce drag on the body but also to provide thermal protection ([6]).

In addition to daunting engineering challenges, some of the phenomena supporting the feasibility of an AJAX type vehicle are fraught with controversy (see, for example, [7]). Resolution of these issues will require extensive experimentation as well as simulation. The latter approach requires integration of several disciplines, including fluid dynamics, electromagnetics, chemical kinetics and molecular physics amongst others. This paper describes a recent effort to integrate the first two of these, within the assumptions that characterize ideal and non-ideal magnetogasdynamics.

In this paper, the Euler and Navier-Stokes equations are solved, according to a finite volume formulation and symmetrical structured discretization, applied to the problem of a blunt body in two-dimensions. The work of [8] is the reference one to present the fluid dynamics and Maxwell equations of electromagnetism based on a conservative and finite volume formalisms. The [9] and the [10] symmetrical schemes are applied to solve the conserved equations. Two types of numerical dissipation models are applied, namely: [11] and [12]. A spatially variable time step procedure is employed aiming to accelerate the convergence of the numerical schemes to the steady state solution. Effective gains in terms of

convergence acceleration are observed with this technique [13-14].

The results have proved that, when the [10] scheme is employed with the [11] dissipation operator, an increase in the shock standoff distance is observed, which guarantees a minor increase in the temperature at the blunt body nose (minor armour problems), and a minor increase in the drag aerodynamic coefficient.

2 Formulation to a Flow Submitted to a Magnetic Field

The Navier-Stokes equations to a flow submitted to a magnetic field in a perfect gas formulation are implemented on a finite volume context and two-dimensional space. The Euler equations are obtained by disregarding of the viscous vectors. These equations in integral and conservative forms can be expressed by:

$$\frac{\partial}{\partial t}\int_V Q\,dV + \int_S \vec{F}\bullet \vec{n}\,dS = 0\,, \qquad (1a)$$

with: $\vec{F} = (E_e - E_v)\vec{i} + (F_e - F_v)\vec{j}\,,$ (1b)

where: Q is the vector of conserved variables, V is the computational cell volume, $\vec{F}$ is the complete flux vector, $\vec{n}$ is the unity vector normal to the flux face, S is the flux area, E_e and F_e are the convective flux vectors or the Euler flux vectors considering the contribution of the magnetic field in the x and y directions, respectively, and E_v and F_v are the viscous flux vectors considering the contribution of the magnetic field in the x and y directions, respectively. The unity vectors $\vec{i}$ and $\vec{j}$ define the system of Cartesian coordinates. The vectors Q, E_e, F_e, E_v and F_v can be defined, according to [8], as follows:

$$Q = \begin{Bmatrix} \rho \\ \rho u \\ \rho v \\ \rho Z \\ B_x \\ B_y \end{Bmatrix},\; E_e = \begin{Bmatrix} \rho u \\ \rho u^2 + P - R_b\,B_x^2/\mu_M \\ \rho uv - R_b\,B_x B_y/\mu_M \\ (\rho Z + P)u - R_b(\vec{V}\bullet\vec{B}/\mu_M)B_x \\ 0 \\ uB_y - vB_x \end{Bmatrix},$$

(2a)

$$F_e = \begin{Bmatrix} \rho v \\ \rho uv - R_b\,B_x B_y/\mu_M \\ \rho v^2 + P - R_b\,B_y^2/\mu_M \\ (\rho Z + P)v - R_b(\vec{V}\bullet\vec{B}/\mu_M)B_y \\ vB_x - uB_y \\ 0 \end{Bmatrix}; \qquad (2b)$$

$$E_v = \begin{Bmatrix} 0 \\ \tau_{xx}/\mathrm{Re} \\ \tau_{xy}/\mathrm{Re} \\ (u\tau_{xx} + v\tau_{xy})/\mathrm{Re} - q_x - q_{J,x} \\ 0 \\ \dfrac{1}{\mathrm{Re}_\sigma}\dfrac{1}{\sigma}\left[\dfrac{\partial}{\partial x}\left(\dfrac{B_y}{\mu_M}\right) - \dfrac{\partial}{\partial y}\left(\dfrac{B_x}{\mu_M}\right)\right] \end{Bmatrix} \text{ and}$$

$$F_v = \begin{Bmatrix} 0 \\ \tau_{xy}/\mathrm{Re} \\ \tau_{yy}/\mathrm{Re} \\ (u\tau_{xy} + v\tau_{yy})/\mathrm{Re} - q_y - q_{J,y} \\ \dfrac{1}{\mathrm{Re}_\sigma}\dfrac{1}{\sigma}\left[\dfrac{\partial}{\partial y}\left(\dfrac{B_x}{\mu_M}\right) - \dfrac{\partial}{\partial x}\left(\dfrac{B_y}{\mu_M}\right)\right] \\ 0 \end{Bmatrix}, \qquad (3)$$

in which: ρ is the fluid density; u and v are the Cartesian components of the velocity vector in the x and y directions, respectively; Z is the flow total energy considering the contribution of the magnetic field; B_x and B_y are the Cartesian components of the magnetic field vector active in the x and y directions, respectively; P is the pressure term considering the magnetic field effect; R_b is the magnetic force number or the pressure number; μ_M is the mean magnetic permeability, with the value $4\pi\times10^{-7}$ T.m/A to the atmospheric air; $\vec{V}$ is the flow velocity vector in Cartesian coordinates; $\vec{B}$ is the magnetic field vector in Cartesian coordinates; the τ's are the components of the viscous stress tensor defined at the Cartesian plane; q_x and q_y are the components of the Fourier heat flux vector in the x and y directions, respectively; $q_{J,x}$ and $q_{J,y}$ are the components of the Joule heat flux vector in the x and y directions, respectively; Re_σ is the magnetic Reynolds number; and σ is the electrical conductivity.

The viscous stresses, in N/m^2, are determined, according to a Newtonian fluid model, by:

$$\tau_{xx} = 2\mu\frac{\partial u}{\partial x} - \frac{2}{3}\mu\left(\frac{\partial u}{\partial x} + \frac{\partial v}{\partial y}\right),\; \tau_{xy} = \mu\left(\frac{\partial u}{\partial y} + \frac{\partial v}{\partial x}\right), \text{ (4a)}$$

$$\tau_{yy} = 2\mu \frac{\partial v}{\partial y} - \frac{2}{3}\mu\left(\frac{\partial u}{\partial x} + \frac{\partial v}{\partial y}\right), \qquad (4b)$$

where μ is the fluid molecular viscosity. In this work, the empiric formula of Sutherland was employed to the calculation of the molecular viscosity (details in [15]).

Z is the total energy defined by:

$$Z = \frac{p}{(\gamma-1)\rho} + \frac{u^2+v^2}{2} + R_b\frac{B^2}{2\mu_M\rho} = \frac{p}{(\gamma-1)\rho} + \frac{u^2+v^2}{2}$$

$$+ R_b\frac{\left(B_x^2+B_y^2\right)}{2\mu_M\rho}. \qquad (5)$$

The pressure term is expressed by:

$$P = p + R_b\frac{B^2}{2\mu_M} = p + R_b\frac{\left(B_x^2+B_y^2\right)}{2\mu_M}. \qquad (6)$$

The magnetic force number or pressure number is determined by:

$$R_b = \frac{B_\infty^2}{\rho_\infty V_\infty^2 \mu_{M,\infty}} = \frac{\left(B_{x,\infty}^2+B_{y,\infty}^2\right)}{\rho_\infty\left(u_\infty^2+v_\infty^2\right)\mu_{M,\infty}}. \qquad (7)$$

The laminar Reynolds number is defined by:

$$\mathrm{Re} = \frac{\rho_\infty V_\infty L}{\mu_\infty}, \qquad (8)$$

in which "∞" represents freestream properties, V_∞ represents the characteristic flow velocity and L is a characteristic length of the studied configuration.

The magnetic Reynolds number is calculated by:

$$\mathrm{Re}_\sigma = L V_\infty \mu_{M,\infty} \sigma_\infty. \qquad (9)$$

The components of the Fourier heat flux vector are expressed by:

$$q_x = -\frac{\mu}{(\gamma-1)\mathrm{Pr}M_\infty^2\mathrm{Re}}\frac{\partial T}{\partial x} \quad \text{and}$$

$$q_y = -\frac{\mu}{(\gamma-1)\mathrm{Pr}M_\infty^2\mathrm{Re}}\frac{\partial T}{\partial y}, \qquad (10)$$

with:

$$\mathrm{Pr} = \mu_\infty Cp/k = 0.72, \text{ is the laminar Prandtl}$$
number; $\qquad (11)$

$$M_\infty = \frac{V_\infty}{\sqrt{\gamma p/\rho}}, \text{ is the freestream Mach number;}$$

$$(12)$$

γ is the ratio of specific heats to a perfect gas, with a value of 1.4 to atmospheric air.

The components of the Joule heat flux vector, which characterizes the non-ideal formulation, are determined by:

$$q_{J,x} = -\frac{R_b}{R_\sigma}\left\{\frac{B_y}{\mu_M\sigma}\left[\frac{\partial}{\partial x}\left(\frac{B_y}{\mu_M}\right) - \frac{\partial}{\partial y}\left(\frac{B_x}{\mu_M}\right)\right]\right\} \quad \text{and}$$

$$q_{J,y} = -\frac{R_b}{R_\sigma}\left\{\frac{B_x}{\mu_M\sigma}\left[\frac{\partial}{\partial y}\left(\frac{B_x}{\mu_M}\right) - \frac{\partial}{\partial x}\left(\frac{B_y}{\mu_M}\right)\right]\right\}. \qquad (13)$$

3 [9] Structured Algorithm in Two-Dimensions

Employing finite volumes and applying the Green theorem to Eq. (1), one writes:

$$\partial Q_{i,j}/\partial t = -1/V_{i,j}\int_S\left(\vec{F}\bullet\vec{n}\right)_{i,j}dS_{i,j}. \qquad (14)$$

In the discretization of the surface integral, Eq. (14) can be rewritten as:

$$dQ_{i,j}/dt = -1/V_{i,j}\left[\left(\vec{F}\bullet\vec{S}\right)_{i,j-1/2} + \left(\vec{F}\bullet\vec{S}\right)_{i+1/2,j} + \right.$$

$$\left.\left(\vec{F}\bullet\vec{S}\right)_{i,j+1/2} + \left(\vec{F}\bullet\vec{S}\right)_{i-1/2,j}\right]. \qquad (15)$$

Discretizing Equation (15) in time employing the explicit Euler method, results in:

$$Q_{i,j}^{n+1} = Q_{i,j}^n - \Delta t_{i,j}/V_{i,j}\left[\left(F\cdot S\right)_{i,j-1/2} + \left(F\cdot S\right)_{i+1/2,j} + \right.$$

$$\left.\left(F\cdot S\right)_{i,j+1/2} + \left(F\cdot S\right)_{i-1/2,j}\right]^n. \qquad (16)$$

The time integration is now divided in two steps: one predictor and another corrector. In the predictor step, the convective flux terms are calculated using the properties of the forward cell in relation to the flux interface. The viscous terms are discretized in a symmetrical form. In the corrector step, the properties of the backward cell in relation to the flux interface are employed. The viscous terms are again

calculated in a symmetrical form. With this procedure, the scheme is of second order accuracy in space and time. Hence, the [9] algorithm, based on a finite volume formulation, is described as follows:

Predictor step:

$$\Delta Q_{i,j}^{\overline{n+1}} = -\Delta t_{i,j}/V_{i,j} \left\{ \left[(E_e)_{i,j} - (E_v)_{i,j-1/2}\right] S_{xi,j-1/2} \right.$$

$$+ \left[(F_e)_{i,j} - (F_v)_{i,j-1/2}\right] S_{yi,j-1/2} + \left[(E_e)_{i+1,j} - (E_v)_{i+1/2,j}\right] S_{xi+1/2,j}$$
$$+ \left[(F_e)_{i+1,j} - (F_v)_{i+1/2,j}\right] S_{yi+1/2,j} + \left[(E_e)_{i,j+1} - (E_v)_{i,j+1/2}\right] S_{xi,j+1/2}$$
$$+ \left[(F_e)_{i,j+1} - (F_v)_{i,j+1/2}\right] S_{yi,j+1/2} + \left[(E_e)_{i,j} - (E_v)_{i-1/2,j}\right] S_{xi-1/2,j}$$
$$+ \left[(F_e)_{i,j} - (F_v)_{i-1/2,j}\right] S_{yi-1/2,j} \right\}^n ; \qquad (17)$$

$$Q_{i,j}^{\overline{n+1}} = Q_{i,j}^n + \Delta Q_{i,j}^{\overline{n+1}}; \qquad (18)$$

Corrector step:

$$\Delta Q_{i,j}^{n+1} = -\Delta t_{i,j}/V_{i,j} \left\{ \left[(E_e)_{i,j-1} - (E_v)_{i,j-1/2}\right] S_{xi,j-1/2} \right.$$

$$+ \left[(F_e)_{i,j-1} - (F_v)_{i,j-1/2}\right] S_{yi,j-1/2} + \left[(E_e)_{i,j} - (E_v)_{i+1/2,j}\right] S_{xi+1/2,j}$$
$$+ \left[(F_e)_{i,j} - (F_v)_{i+1/2,j}\right] S_{yi+1/2,j} + \left[(E_e)_{i,j} - (E_v)_{i,j+1/2}\right] S_{xi,j+1/2}$$
$$+ \left[(F_e)_{i,j} - (F_v)_{i,j+1/2}\right] S_{yi,j+1/2} + \left[(E_e)_{i-1,j} - (E_v)_{i-1/2,j}\right] S_{xi-1/2,j}$$
$$+ \left[(F_e)_{i-1,j} - (F_v)_{i-1/2,j}\right] S_{yi-1/2,j} \right\}^{\overline{n+1}} ; \qquad (19)$$

$$Q_{i,j}^{n+1} = 0.5\left(Q_{i,j}^n + Q_{i,j}^{\overline{n+1}} + \Delta Q_{i,j}^{n+1}\right). \qquad (20)$$

With the intent of guaranteeing numerical stability to the [9] scheme, in its two-dimensional version, an artificial dissipation operator of second and fourth differences ([16-17]) is subtracted from the flux terms of the right side (RHS, "Right Hand Side") in the corrector step, aiming to eliminate instabilities originated from shock waves and due to the field stability. The operator is of the following type: $D_{i,j} = d_{i,j}^{(2)} - d_{i,j}^{(4)}$, defined in subsection 4.1.

4 [10] Structured Algorithm in Two-Dimensions

Equation (1) can be rewritten following a structured spatial discretization context ([18] and [10]) as:

$$d\left(V_{i,j}Q_{i,j}\right)/dt + C(Q_{i,j}) = 0, \qquad (21)$$

where:

$$C(Q_{i,j}) = \left\{0.5\left[(E_e)_{i,j} + (E_e)_{i,j-1}\right] - (E_v)_{i,j-1/2}\right\} S_{xi,j-1/2}$$

$$+ \left\{0.5\left[(F_e)_{i,j} + (F_e)_{i,j-1}\right] - (F_v)_{i,j-1/2}\right\} S_{yi,j-1/2}$$

$$+ \left\{0.5\left[(E_e)_{i,j} + (E_e)_{i+1,j}\right] - (E_v)_{i+1/2,j}\right\} S_{xi+1/2,j}$$

$$+ \left\{0.5\left[(F_e)_{i,j} + (F_e)_{i+1,j}\right] - (F_v)_{i+1/2,j}\right\} S_{yi+1/2,j}$$

$$+ \left\{0.5\left[(E_e)_{i,j} + (E_e)_{i,j+1}\right] - (E_v)_{i,j+1/2}\right\} S_{xi,j+1/2}$$

$$+ \left\{0.5\left[(F_e)_{i,j} + (F_e)_{i,j+1}\right] - (F_v)_{i,j+1/2}\right\} S_{yi,j+1/2}$$

$$+ \left\{0.5\left[(E_e)_{i,j} + (E_e)_{i-1,j}\right] - (E_v)_{i-1/2,j}\right\} S_{xi-1/2,j}$$

$$+ \left\{0.5\left[(F_e)_{i,j} + (F_e)_{i-1,j}\right] - (F_v)_{i-1/2,j}\right\} S_{yi-1/2,j}$$

$$(22)$$

is the approximation to the flux integral of Eq. (1). In this work, one adopts that, for example, the flux vector E_e at the flux interface (i,j-1/2) is obtained by the arithmetical average between the E_e vector calculated at the cell (i,j) and the E_e vector calculated at the cell (i,j-1). The viscous flux vectors are calculated in a symmetrical form as demonstrated in section 5.

The spatial discretization proposed by the authors is equivalent to a symmetrical scheme with second order accuracy, on a finite difference context. The introduction of an artificial dissipation operator "D" is necessary to guarantee the scheme numerical stability in presence of, for example, uncoupled odd/even solutions and non-linear stabilities, as shock waves. Equation (21) can, so, be rewritten as:

$$d\left(V_{i,j}Q_{i,j}\right)/dt + \left[C(Q_{i,j}) - D(Q_{i,j})\right] = 0. \qquad (23)$$

The time integration is performed by a hybrid Runge-Kutta method of five stages, with second order accuracy, and can be represented in general form as:

$$Q_{i,j}^{(0)} = Q_{i,j}^{(n)}$$
$$Q_{i,j}^{(k)} = Q_{i,j}^{(0)} - \alpha_k \Delta t_{i,j}/V_{i,j}\left[C\left(Q_{i,j}^{(k-1)}\right) - D\left(Q_{i,j}^{(m)}\right)\right], \quad (24)$$
$$Q_{i,j}^{(n+1)} = Q_{i,j}^{(k)}$$

where: k = 1,...,5; m = 0 until 4; $\alpha_1 = 1/4$, $\alpha_2 = 1/6$, $\alpha_3 = 3/8$, $\alpha_4 = 1/2$ and $\alpha_5 = 1$. [10] suggest that the artificial dissipation operator should be evaluated only in the first two stages as the Euler equations were solved (m = 0, k = 1 and m = 1, k = 2). [19] suggest that the artificial dissipation operator should be evaluated in alternated stages as the Navier-Stokes equations were solved (m = 0, k = 1, m = 2, k = 3 and m = 4, k = 5). These procedures aim CPU time economy and also better damping of the numerical instabilities originated from the discretization based on the hyperbolic characteristics of the Euler equations and the hyperbolic/parabolic characteristics of the Navier-Stokes equations.

4.1 Artificial dissipation operator

The artificial dissipation operator implemented in the [9] and in the [10] schemes has the following structure:

$$D\big(Q_{i,j}\big) = d^{(2)}\big(Q_{i,j}\big) - d^{(4)}\big(Q_{i,j}\big), \qquad (25)$$

where:

$$
\begin{aligned}
d^{(2)}\big(Q_{i,j}\big) = {} & 0.5\varepsilon_{i,j-1/2}^{(2)}\big(A_{i,j} + A_{i,j-1}\big)\big(Q_{i,j-1} - Q_{i,j}\big) \\
& + 0.5\varepsilon_{i+1/2,j}^{(2)}\big(A_{i,j} + A_{i+1,j}\big)\big(Q_{i+1,j} - Q_{i,j}\big) \\
& + 0.5\varepsilon_{i,j+1/2}^{(2)}\big(A_{i,j} + A_{i,j+1}\big)\big(Q_{i,j+1} - Q_{i,j}\big) \\
& + 0.5\varepsilon_{i-1/2,j}^{(2)}\big(A_{i,j} + A_{i-1,j}\big)\big(Q_{i-1,j} - Q_{i,j}\big)
\end{aligned}
$$

$$(26)$$

named undivided Laplacian operator, is responsible by the numerical stability in the presence of shock waves; and

$$
\begin{aligned}
d^{(4)}\big(Q_{i,j}\big) = {} & 0.5\varepsilon_{i,j-1/2}^{(4)}\big(A_{i,j} + A_{i,j-1}\big)\big(\nabla^2 Q_{i,j-1} - \nabla^2 Q_{i,j}\big) \\
& + 0.5\varepsilon_{i+1/2,j}^{(4)}\big(A_{i,j} + A_{i+1,j}\big)\big(\nabla^2 Q_{i+1,j} - \nabla^2 Q_{i,j}\big) \\
& + 0.5\varepsilon_{i,j+1/2}^{(4)}\big(A_{i,j} + A_{i,j+1}\big)\big(\nabla^2 Q_{i,j+1} - \nabla^2 Q_{i,j}\big) \\
& + 0.5\varepsilon_{i-1/2,j}^{(4)}\big(A_{i,j} + A_{i-1,j}\big)\big(\nabla^2 Q_{i-1,j} - \nabla^2 Q_{i,j}\big),
\end{aligned}
$$

$$(27)$$

named bi-harmonic operator, is responsible by the background stability (for example: instabilities originated from uncoupled odd/even solutions). In this last term,

$$
\begin{aligned}
\nabla^2 Q_{i,j} = {} & \big(Q_{i,j-1} - Q_{i,j}\big) + \big(Q_{i+1,j} - Q_{i,j}\big) \\
& + \big(Q_{i,j+1} - Q_{i,j}\big) + \big(Q_{i-1,j} - Q_{i,j}\big). \qquad (28)
\end{aligned}
$$

In the $d^{(4)}$ operator, $\nabla^2 Q_{i,j}$ is extrapolated from the value of the real neighbor cell every time that it represent a ghost cell. The ε terms are defined, for example, as:

$$\varepsilon_{i,j-1/2}^{(2)} = K^{(2)} MAX \; \big(v_{i,j}, v_{i,j-1}\big) \quad \text{and}$$

$$\varepsilon_{i,j-1/2}^{(4)} = MAX \; \big[0, \big(K^{(4)} - \varepsilon_{i,j-1/2}^{(2)}\big)\big], \qquad (29)$$

with:

$$v_{i,j} = \Big(\big|p_{i,j-1} - p_{i,j}\big| + \big|p_{i+1,j} - p_{i,j}\big| + \big|p_{i,j+1} - p_{i,j}\big| + \big|p_{i-1,j} - p_{i,j}\big|\Big) \Big/$$

$$\big(p_{i,j-1} + p_{i+1,j} + p_{i,j+1} + p_{i-1,j} + 4p_{i,j}\big) \qquad (30)$$

representing a pressure sensor employed to identify regions of elevated gradients. The $K^{(2)}$ and $K^{(4)}$ constants has typical values of 1/4 and 3/256, respectively. Every time that a neighbor cell represents a ghost cell, one assumes, for example, that $v_{ghost} = v_{i,j}$. The $A_{i,j}$ terms can be defined according to two models implemented in this work: (a) [11] and (b) [12]. In the first case, the $A_{i,j}$ terms are contributions from the maximum normal eigenvalue of the Euler equations integrated along each cell face. Hence, they are defined as follows:

(a) [11] model:

$$
\begin{aligned}
A_{i,j} = {} & \Big[\big|0.5\big(u_{i,j} + u_{i,j-1}\big)S_{x_{i,j-1/2}} + 0.5\big(v_{i,j} + v_{i,j-1}\big)S_{y_{i,j-1/2}}\big|\Big] \\
& + 0.5\big(a_{i,j} + a_{i,j-1}\big)\big(S_{x_{i,j-1/2}}^2 + S_{y_{i,j-1/2}}^2\big)^{0.5} + \\
& \Big[\big|0.5\big(u_{i,j} + u_{i+1,j}\big)S_{x_{i+1/2,j}} + 0.5\big(v_{i,j} + v_{i+1,j}\big)S_{y_{i+1/2,j}}\big|\Big] \\
& + 0.5\big(a_{i,j} + a_{i+1,j}\big)\big(S_{x_{i+1/2,j}}^2 + S_{y_{i+1/2,j}}^2\big)^{0.5} +
\end{aligned}
$$

$$(31a)$$

$$\Big[\Big|0.5\big(u_{i,j} + u_{i,j+1}\big)S_{x_{i,j+1/2}} + 0.5\big(v_{i,j} + v_{i,j+1}\big)S_{y_{i,j+1/2}}\Big|\Big]$$

$$+ 0.5\big(a_{i,j} + a_{i,j+1}\big)\Big(S^2_{x_{i,j+1/2}} + S^2_{y_{i,j+1/2}}\Big)^{0.5} +$$

$$\Big[\Big|0.5\big(u_{i,j} + u_{i-1,j}\big)S_{x_{i-1/2,j}} + 0.5\big(v_{i,j} + v_{i-1,j}\big)S_{y_{i-1/2,j}}\Big|\Big]$$

$$+ 0.5\big(a_{i,j} + a_{i-1,j}\big)\Big(S^2_{x_{i-1/2,j}} + S^2_{y_{i-1/2,j}}\Big)^{0.5}, \qquad (31b)$$

where "a" represents the sound speed.

(b) [12] model:

$$A_{i,j} = V_{i,j}\big/\Delta t_{i,j}, \qquad (32)$$

which represents a scaling factor, according to structured meshes, with the desired behavior to the artificial dissipation term: (i) bigger control volumes result in bigger value to the dissipation term; (ii) smaller time steps also result in bigger values to the scaling term.

5 Calculations of the Viscous Gradients

The viscous vectors at the flux interface are obtained by the arithmetical average between the primitive variables at the right and left states of the flux interface, as also the arithmetical average of the primitive variable gradients, also considering the right and left states of the flux interface. The gradients of the primitive variables present in the viscous flux vectors are calculated employing the Green theorem, which considers that the gradient of a primitive variable is constant in the volume and that the volume integral which defines this gradient is replaced by a surface integral. This methodology to calculation of the viscous gradients is based on the work of [20]. As an example, one has to $\partial u/\partial x$:

$$\frac{\partial u}{\partial x} = \frac{1}{V}\int_V \frac{\partial u}{\partial x}\,dV = \frac{1}{V}\int_S u\big(\vec{n}\bullet d\vec{S}\big) = \frac{1}{V}\int_{S_x} u\,dS_x \cong$$

$$\frac{1}{V_{i,j}}\Big[0.5\big(u_{i,j} + u_{i,j-1}\big)S_{x_{i,j-1/2}} + 0.5\big(u_{i,j} + u_{i+1,j}\big)S_{x_{i+1/2,j}}$$

$$+ 0.5\big(u_{i,j} + u_{i,j+1}\big)S_{x_{i,j+1/2}} + 0.5\big(u_{i,j} + u_{i-1,j}\big)S_{x_{i-1/2,j}}\Big].$$

$$(33)$$

The dimensionless employed in the Euler and Navier-Stokes equations, the boundary conditions, the geometry configuration and the employed meshes are presented in [21].

6 Dimensionless, Initial and Boundary Conditions, Computational Domain and Employed Meshes

6.1 Dimensionless

The dimensionless employed to the case of the flowfield submitted to a magnetic field in two-dimensions are detailed as follows: ρ is dimensionless in relation to ρ_∞; the u and v Cartesian components of velocity are dimensionless in relation to the freestream speed of sound, a_∞; p is dimensionless in relation to the product between ρ_∞ and the squared of a_∞; the translational/rotational temperature is dimensionless in relation to a_∞; the molecular viscosity is dimensionless in relation to μ_∞; the Cartesian components of the induced magnetic field is dimensionless by B_∞; the magnetic permeability of the mean is dimensionless by $\mu_{M,\infty}$; and the electric conductivity is dimensionless by σ_∞.

6.2 Initial and boundary conditions

6.2.1 Initial condition

The initial condition adopts freestream flow properties to the conserved variables. Due to the present dimensionless, the vector of conserved variables in the field is determined as follows:

$$Q = \left\{\begin{array}{c} 1.0 \\ M_\infty \cos\theta \\ M_\infty \sin\theta \\ \dfrac{1}{\gamma(\gamma-1)} + 0.5M_\infty^2 + 0.5R_b \\ B_{x,\infty}\,/\,B_\infty \\ B_{y,\infty}\,/\,B_\infty \end{array}\right\}, \qquad (34)$$

where θ is the angle of attack, M_∞ is the freestream Mach number, $B_{x,\infty}$, $B_{y,\infty}$, B_∞ are the Cartesian components of the induced magnetic field and the modulus of the induced magnetic field, and R_b is calculated according to Eq. (7).

6.2.2 Boundary conditions

The boundary conditions are basically of three types: solid wall, entrance and exit. These

conditions are implemented in special cells named "ghost cells".

(a) Solid wall condition: In the inviscid case, this condition imposes the flow tangency at wall. This condition is satisfied considering the velocity component tangent to the wall relative to the ghost cell as equal to the respective component of the real neighbor cell. At the same time, the velocity component normal to the wall relative to the ghost cell is equaled to the negative of the respective component of the real neighbor cell. This procedure leads to a system of equations which results to:

$$u_g = \left(n_y^2 - n_x^2\right)u_r + \left(-2n_x n_y\right)v_r \quad \text{and}$$
$$v_g = \left(-2n_x n_y\right)u_r + \left(n_x^2 - n_y^2\right)v_r, \tag{35}$$

where "g" indicate ghost cell properties and "r" indicate real cell properties. In the viscous case, the Cartesian components of the velocity vector of the ghost cells are equaled in value, but with the opposed signal, with the respective Cartesian components of the real cell.

$$u_g = -u_r \quad \text{and} \quad v_g = -v_r. \tag{36}$$

In both cases, inviscid and viscous, the pressure gradient normal to the wall is equaled to zero, according to an inviscid formulation in the former case and to the boundary layer condition in the latter. The same hypothesis is employed to the temperature gradient normal to the wall, considering an adiabatic wall. With these conditions, ghost cell density and pressure are extrapolated from the respective values of the real neighbor cell (zero order extrapolation).

The Cartesian components of the induced magnetic field at the wall to the ghost cells are fixed with their initial values. The magnetic permeability is considered constant with its initial value. The total energy Z to the ghost cell is calculated by:

$$Z_g = \frac{p_g}{(\gamma - 1)\rho_g} + 0.5\left(u_g^2 + v_g^2\right) + 0.5R_b \frac{B_{x,g}^2 + B_{y,g}^2}{\mu_{M,g}\rho_g}. \tag{37}$$

(b) Entrance condition:
(b.1) Subsonic flow: Five properties are specified and one is extrapolated, based on the analysis of information propagation along the characteristic directions in the calculation domain ([21]). In other words, five characteristic directions of information propagation points to inside the computational

domain and should be specified, to the subsonic flow. Only the characteristic direction associated with the "$(q_n\text{-}a)$" eigenvalue cannot be specified and should be determined by interior information of the calculation domain. The pressure is the extrapolated variable from the real neighbor cell. Density, Cartesian velocity components and Cartesian induced magnetic field components have their values determined by the initial condition. The total energy is determined by Eq. (37).

(b.2) Supersonic flow: All variables are fixed with their initial values.

(c) Exit condition:
(c.1) Subsonic flow: Five characteristic directions of information propagation points outward from the computational domain and should be extrapolated from the interior information. The characteristic direction associated with the eigenvalue "$(q_n\text{-}a)$" should be specified because points inward the calculation domain ([21]). In this case, the ghost cell pressure is specified by its initial value. Density, Cartesian velocity components and Cartesian induced magnetic field components are extrapolated and the total energy is determined by Eq. (37).

(c.2) Supersonic flow: All variables are extrapolated from the interior domain due to the fact that all six characteristic directions of information propagation of the Euler equations point outward from the calculation domain and, with it, nothing can be fixed.

6.3 Computational domain
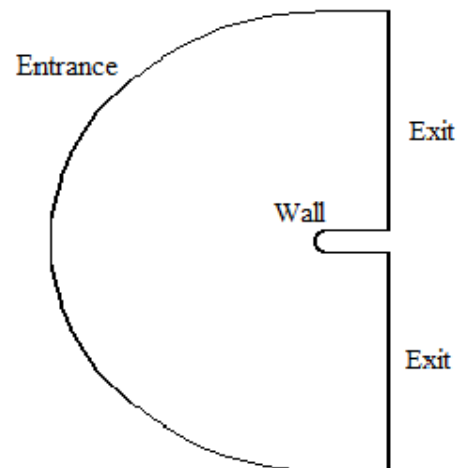
Figure 1 : Blunt body computational domain.

Figure 1 presents the geometry and the computational domain employed in the structured simulations in two-dimensions. This figure describes a blunt body with nose ratio of 1.0m and the far field located at twenty times the nose ratio in

relation to the configuration nose. The domain presents three frontiers, as related in the boundary conditions, namely: solid wall, entrance and exit.

6.4 Employed meshes
Figures 2 and 3 present the meshes employed to the structured simulations in two-dimensions for the case of a flow submitted to an induced magnetic field around a blunt body.
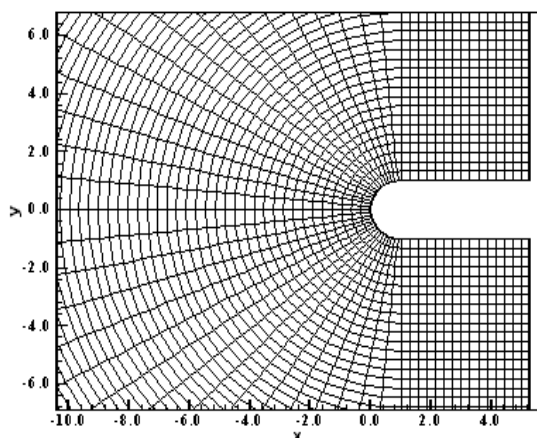

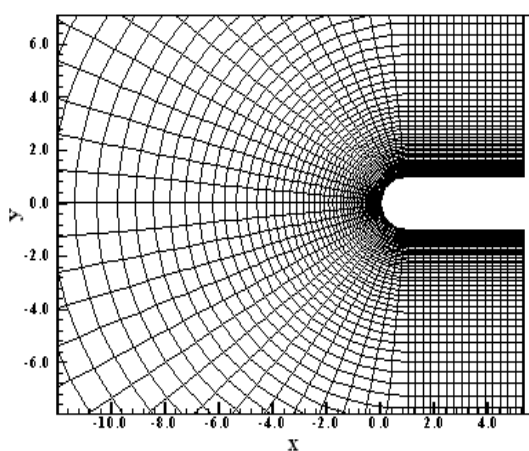
Figure 2 : Structured mesh to the inviscid 2D case.

Figure 3 : Structured mesh to the viscous 2D case.

Figure 2 exhibits the mesh used to the inviscid simulations and Fig. 3 the mesh to the viscous simulations. The mesh to the viscous case presents an exponential stretching in the η direction of 7.5%. The mesh to the inviscid case is composed of 3,658 rectangular cells and 3,780 nodes, which corresponds to a finite difference mesh of 63x60 points. The mesh to the viscous case is composed by the same number of cells and nodes, also corresponding to a mesh of 63x60 points.

7 Results
Tests were performed in three microcomputers: one with processor INTEL CELERON, 1.5GHz of clock and 1.0GBytes of RAM (notebook), the second with processor AMD SEMPRON (tm) 2600+, 1.83GHz of clock and 512 Mbytes of RAM (desktop), and the third one with processor INTEL CELERON 2.13GHz of clock and 1.0GBytes of RAM (notebook). As the interest of this work is steady state problems, one needs to define a criterion which guarantees that such condition was reached. The criterion adopted in this work was to consider a reduction of no minimal three (3) orders in the magnitude of the maximum residual in the domain, a typical criterion in the CFD community. The residual to each cell was defined as the numerical value obtained from the discretized conservation equations. As there are six (6) conservation equations to each cell, the maximum value obtained from these equations is defined as the residual of this cell. Thus, this residual is compared with the residual of the other cells, calculated of the same way, to define the maximum residual in the domain. In the simulations, the attack angle, α, was set equal to zero.

7.1 Initial conditions
The initial conditions to the standard simulation of the studied algorithms are presented in Tab. 1. This is a standard case to the ideal gas flow submitted to a magnetic field normal to the symmetry line of the configuration under study. The Reynolds number was calculated from the data of [22].

Table 1 : Initial conditions of the simulations in 2D.

Property	Value
M_∞	10.6
$B_{y,\infty}$	0.15 T
μ_M	1.2566×10^{-6} T.m/A
σ_∞	1,000 ohm/m
Altitude	40,000 m
Pr	0.72
L (2D)	2.0 m
Re_∞ (2D)	1.6806×10^6

7.2. Numerical results

7.2.1 Grid independent solution
Before start the presentation of the results, a computational grid independence study was performed. Four different meshes were analyzed: 43x40, 53x50, 63x60 and 73x70. The

reference parameter chosen to indicate grid independent solution was the –Cp distribution around the blunt body, considering the inviscid case. The scheme to determine this solution was the [9] one and the [11] artificial dissipation operator was employed. The studied meshes are presented in Figs. 4 to 7 and the –Cp distributions are presented in Fig. 8.
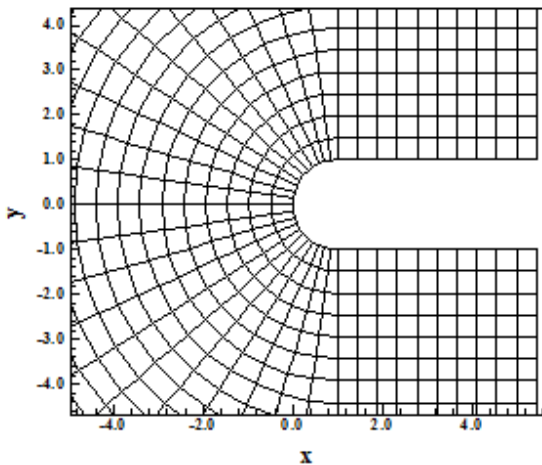
Figure 4 : Mesh of 43x40 points.
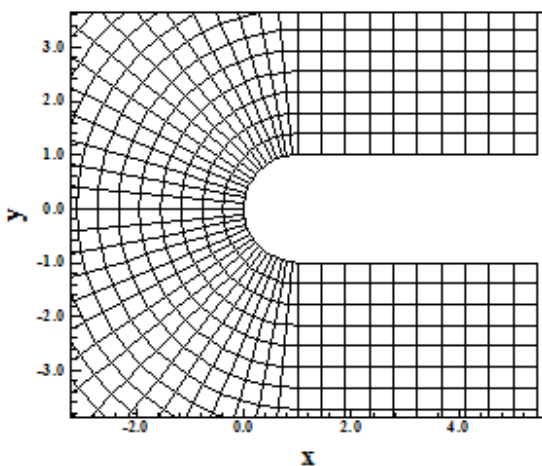
Figure 5 : Mesh of 53x50 points.

It is clear from Fig. 8 that the grid dependent solution is obtained with mesh 63x60. The differences between meshes 63x60 and 73x70 are minimal. So, the mesh of 63x60 points was chose for the numerical experiments performed in this work. To the viscous experiments, it was employed the same mesh, with the exponential stretching referred in section **6.4**.
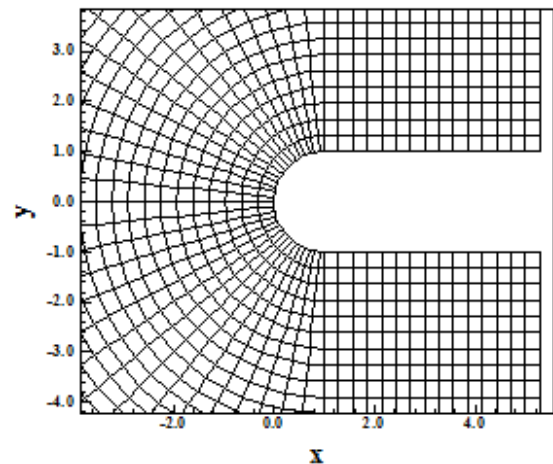
Figure 6 : Mesh of 63x60 points.
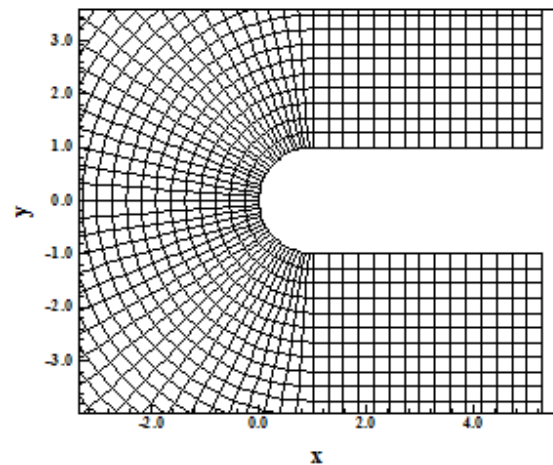
Figure 7 : Mesh of 73x70 points.
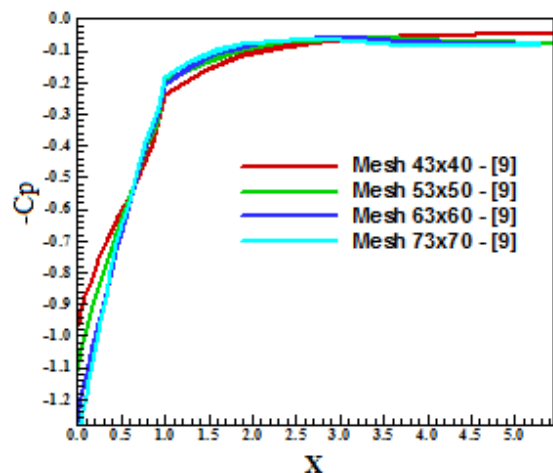
Figure 8 : -Cp distributions – Grid independent solution.

7.2.2 Results with the [9] scheme to inviscid flow in two-dimensions

Figures 9 and 10 present the pressure contours calculated at the computational domain to the ideal gas flow, inviscid, submitted to a magnetic field.

Figures 9 and 10 exhibit the solutions obtained with the [9] scheme employing the artificial dissipation models of [12] and of [11], respectively. The pressure field obtained by the [9] scheme employing the dissipation model of [11] is more intense than that obtained with the dissipation model of [12]. Good symmetry properties are observed in both solutions.
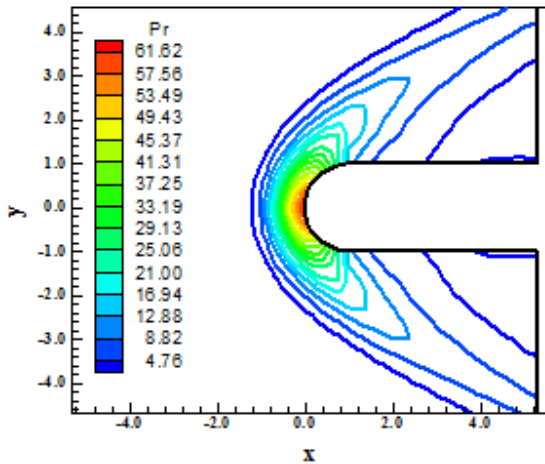
Figure 9 : Pressure contours (Mac/A).
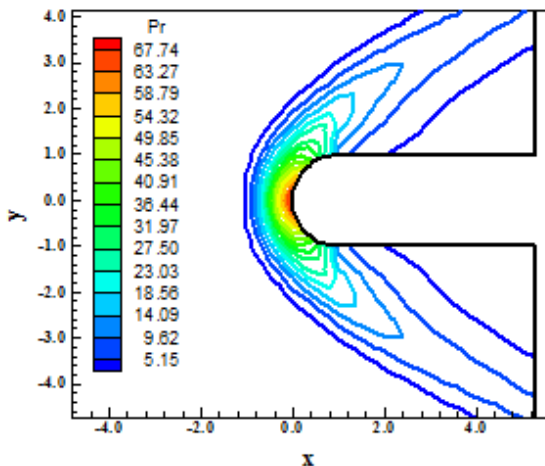
Figure 10 : Pressure contours (Mac/M).

Figures 11 and 12 show the Mach number contours calculated at the computational domain by the [9] scheme employing the artificial dissipation models of [12] and of [11], respectively. The Mach number field obtained by the [9] scheme employing the dissipation model of [11] is more intense. Good symmetry properties are observed in both solutions. The shock wave develops naturally, passing from a normal shock at the symmetry line to oblique shock waves along the body and finishing in a Mach wave, far from the geometry.

Figures 13 and 14 present the translational / rotational temperature distributions calculated at the

computational domain. The [9] scheme with the artificial dissipation model of [12] predicts a more severe temperature field.
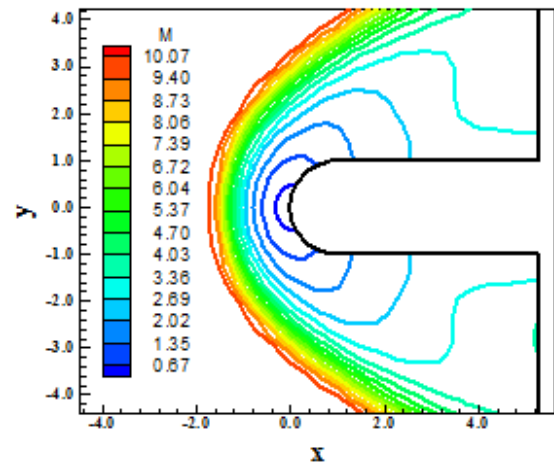
Figure 11 : Mach number contours (Mac/A).
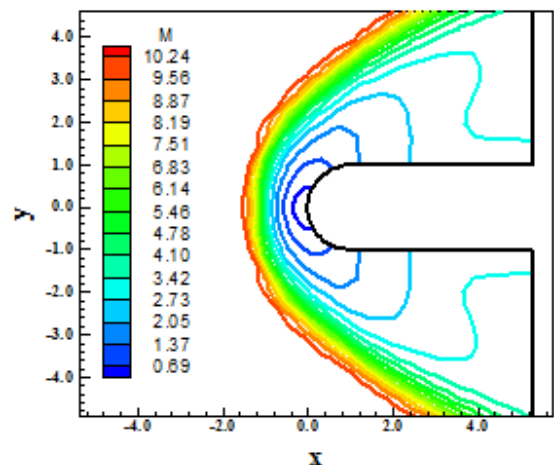
Figure 12 : Mach number contours (Mac/M).
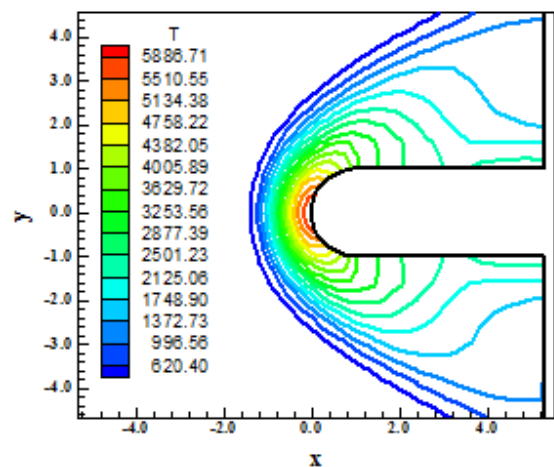
Figure 13 : Temperature contours (Mac/A).

Figures 15 and 16 exhibit the contours of the B_x component of the magnetic field vector determined

at the calculation domain. As can be observed, the B_x component is negative at the geometry lower surface and positive at the geometry upper surface, indicating that the magnetic field performs a curve around the geometry. The solution presented by the [9] scheme with the dissipation model of [11] is quantitatively more symmetrical than the respective one obtained with the dissipation model of [12], although the latter presents a more intense B_x component field.
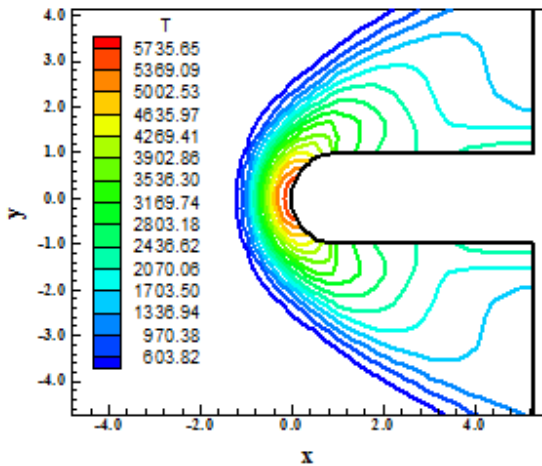
Figure 14 : Temperature contours (Mac/M).
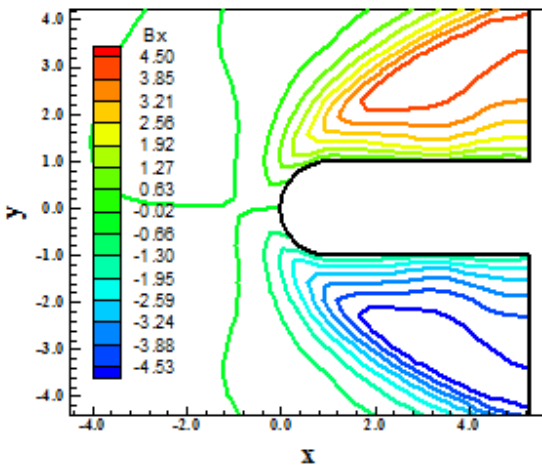
Figure 15 : B_x component of magnetic field (Mac/A).

Figures 17 and 18 exhibit the magnetic vector field with induction lines to highlight the satisfied initial condition far ahead of the configuration and the distortion in these lines close to the blunt body. As can be observed, the magnetic induction lines are initially attracted to the magnetic field imposed at the blunt body walls and, close to the body, suffer distortion, getting round the configuration.
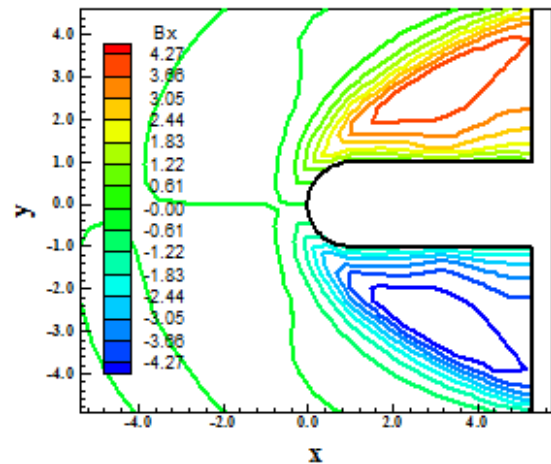
Figure 16 : B_x component of magnetic field (Mac/M).
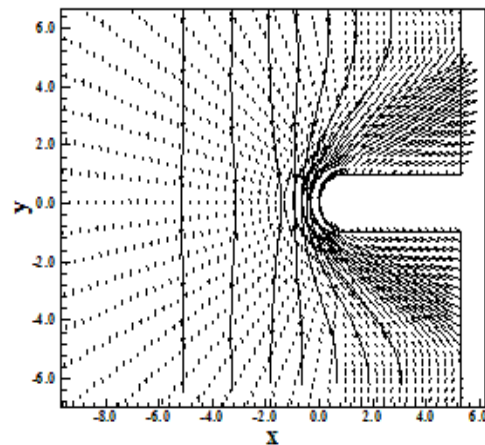
Figure 17 : Magnetic field and induction lines (Mac/A).
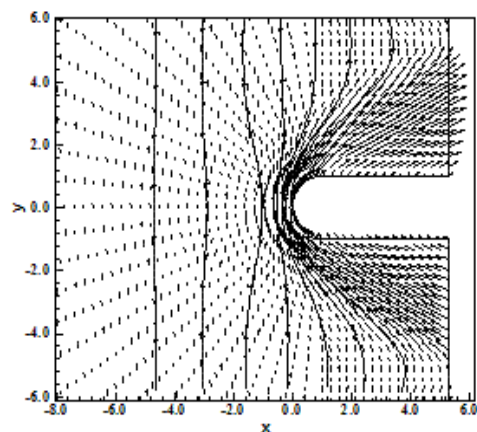
Figure 18 : Magnetic field and induction lines (Mac/M).
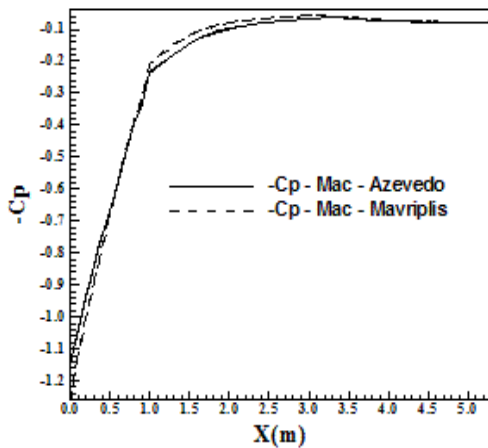
Figure 19 : -Cp distributions.

Figure 19 shows the –Cp distributions along the blunt body wall. As can be seen, the shock captured by the [9] scheme employing the dissipation model of [11] is more severe than that obtained with the dissipation model of [12], presenting a Cp peak at the configuration nose bigger. Figure 20 presents the distribution of the translational / rotational temperature along the configuration symmetry line or configuration stagnation line. As can be noted, the dissipation models predict different shock wave positions. The [12] model predicts the shock wave at 1.85m ahead of the blunt body nose, while the [11] model predicts the shock wave at 1.55m ahead of the blunt body nose.
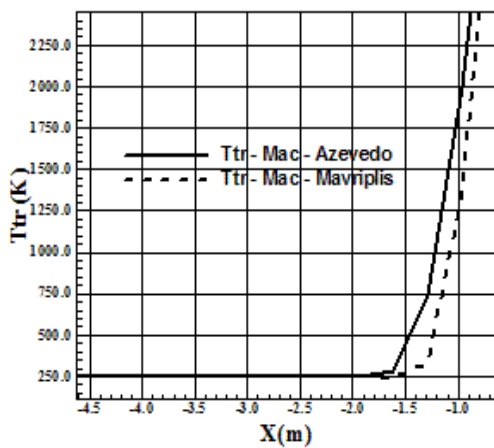
Figure 20 : Shock position by the temperature profile.

7.2.3 Results with the [9] scheme to viscous flow in two-dimensions
Figures 21 and 22 exhibit the pressure contours calculated at the computational domain. The pressure field obtained by the [9] scheme employing the dissipation model of [12] is more intense than that obtained with the dissipation model of [11],

with a behavior opposed to that observed in the inviscid solution. Good symmetry properties are observed in both solutions.
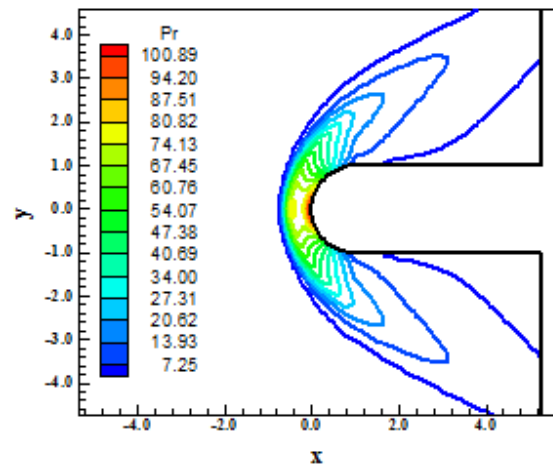
Figure 21 : Pressure contours (Mac/A).
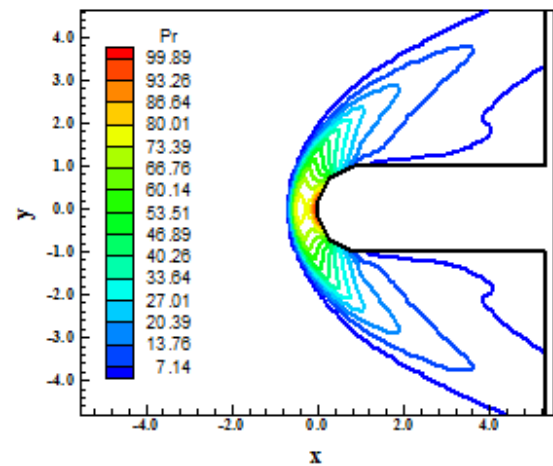
Figure 22 : Pressure contours (Mac/M).
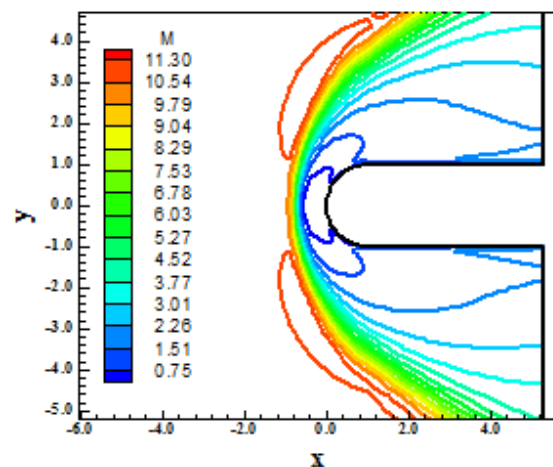
Figure 23 : Mach number contours (Mac/A).

Figures 23 and 24 show the Mach number contours calculated at the computational domain by

the [9] scheme employing the artificial dissipation models of [12] and of [11], respectively. The Mach number field obtained by the [9] scheme employing the dissipation model of [11] is more intense. It is important to note that both solutions present pre-shock oscillation problems, being more critical those observed in the solution with [11] model. Good symmetry properties are observed in both solutions.

B_x component is negative at the geometry lower surface and positive at the geometry upper surface, indicating that the magnetic field performs a curve around the geometry. The solutions presented by the [9] scheme with the dissipation models of [12] and of [11] have meaningful numerical non-symmetry. The dissipation model of [12] presents a B_x field more intense.
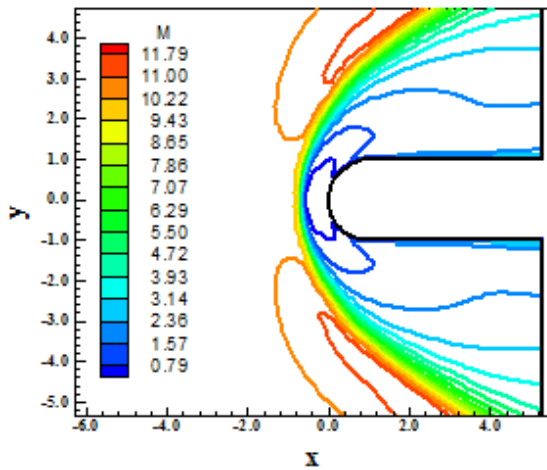
Figure 24 : Mach number contours (Mac/M).
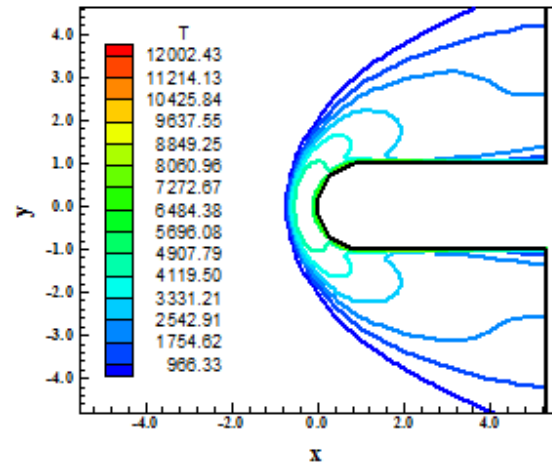
Figure 26 : Temperature contours (Mac/M).

Figure 25 : Temperature contours (Mac/A).
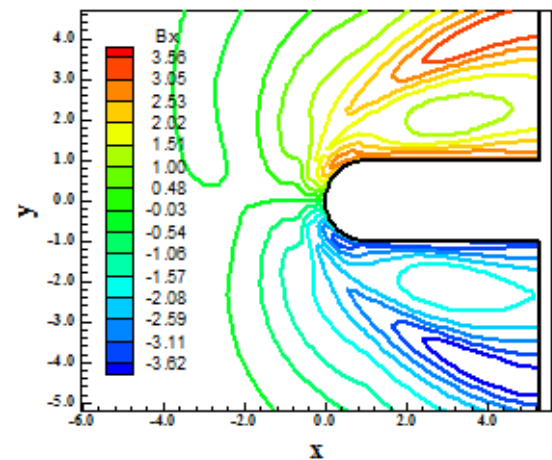
Figure 27 : B_x component of magnetic field (Mac/A).

Figures 25 and 26 present the translational / rotational temperature distributions calculated at the computational domain. The [9] scheme with the artificial dissipation model of [12] predicts a more severe temperature field. This temperature field is much more severe than that obtained by the inviscid solution. The temperature peak occurs along the rectilinear walls, by the development of the wall heating due to the consideration of viscous effects.

Figures 27 and 28 exhibit the contours of the B_x component of the magnetic field vector determined at the calculation domain. As can be observed, the

Figures 29 and 30 exhibit the magnetic vector field with induction lines to highlight the satisfied initial condition far ahead of the configuration and the distortion in these lines close to the blunt body. As can be observed, the magnetic induction lines are initially attracted to the magnetic field imposed at the blunt body walls and, close to the body, suffer distortion, getting round the configuration.

Figure 31 shows the –Cp distributions along the blunt body wall. As can be seen, the shock captured by the [9] scheme employing the dissipation model of [11] is more severe than that obtained with the dissipation model of [12], presenting a Cp variation
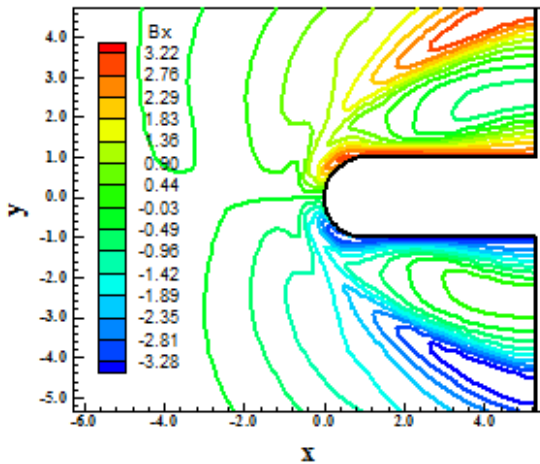
between the configuration nose and the configuration rectilinear walls bigger.

Figure 28 : B_x component of magnetic field (Mac/M).

Figure 29 : Magnetic field and induction lines (Mac/A).

Figura 30 : Magnetic field and induction lines (Mac/M).
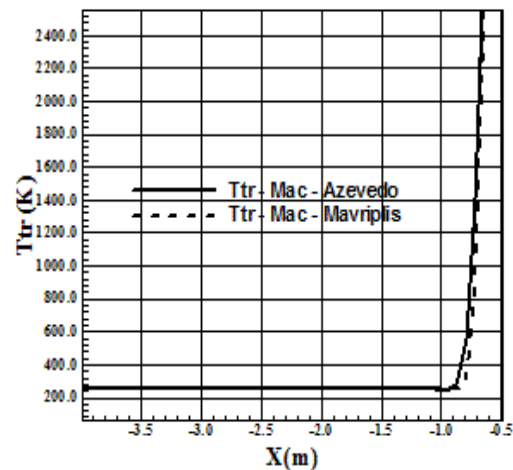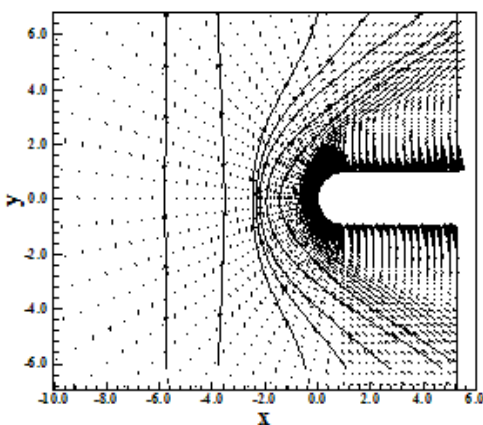
Figure 32 presents the distribution of the translational / rotational temperature along the configuration symmetry line or configuration stagnation line. As can be noted, the dissipation

models predict different shock wave positions. The [12] model predicts the shock wave at 0.90m ahead of the blunt body nose, while the [11] model predicts the shock wave at 0.80m ahead of the blunt body nose.

Figure 31 : -Cp distributions.

Figure 32 : Shock position by the temperature profile.

7.2.4 Results with the [10] scheme to inviscid flow in two-dimensions

Figure 33 and 34 present the pressure contours calculated at the computational domain. The pressure contours obtained by the [10] scheme employing the dissipation model of [11] is more intense than that obtained with the dissipation model of [12]. Good symmetry properties are observed in both solutions.

Figures 35 and 36 exhibit the Mach number contours calculated at the computational domain by the [10] scheme employing the artificial dissipation models of [12] and of [11], respectively. The Mach number field obtained by the [10] scheme employing the dissipation model of [12] is more intense. Good symmetry properties are observed in

both solutions. The shock wave develops naturally, passing from a normal shock (frontal) to a Mach wave, through oblique shock waves.
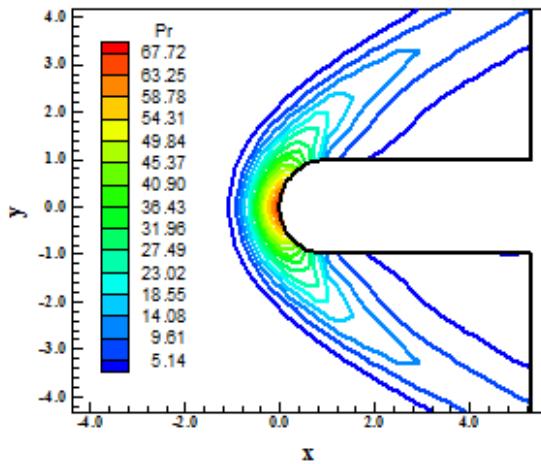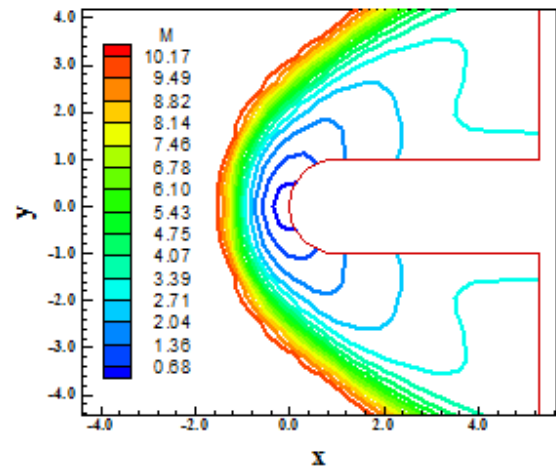

Figure 33 : Pressure contours (JM/A).
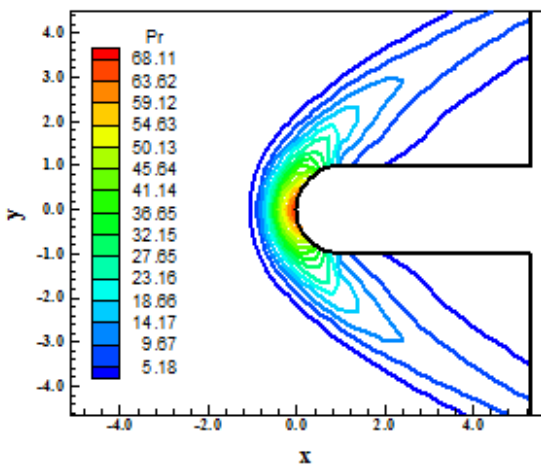

Figure 34 : Pressure contours (JM/M).

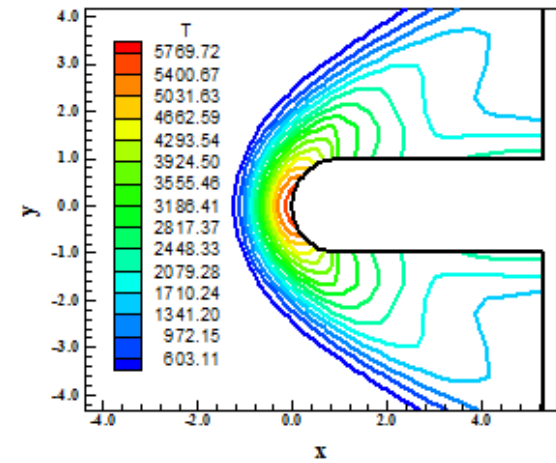Figure 35 : Mach number contours (JM/A).
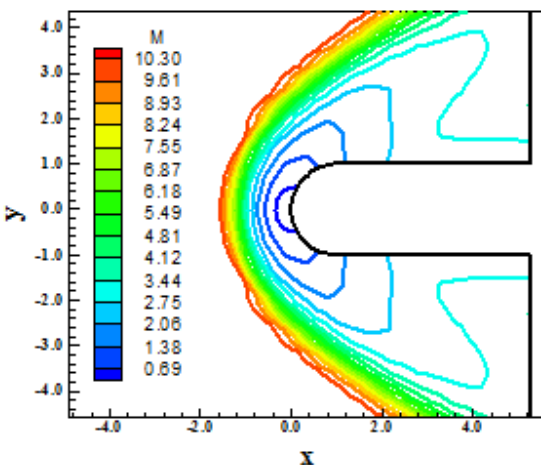

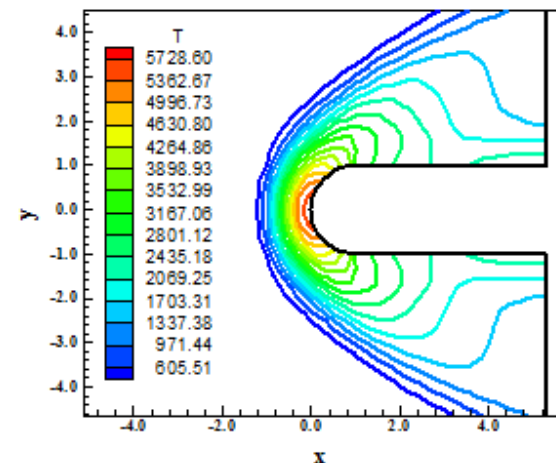Figure 36 : Mach number contours (JM/M).

Figure 37 : Temperature contours (JM/A).

Figure 38 : Temperature contours (JM/M).

Figures 37 and 38 show the translational / rotational temperature distributions calculated at the computational domain. The [10] scheme with the artificial dissipation model of [12] predicts a more

severe temperature field. This field is, however, inferior in intensity to the respective one calculated by the [9] scheme, as seen in Fig. 13.

the blunt body walls and, close to the body, suffer distortion, getting round the configuration. The same behavior was observed in the inviscid solutions obtained with the [9] scheme.
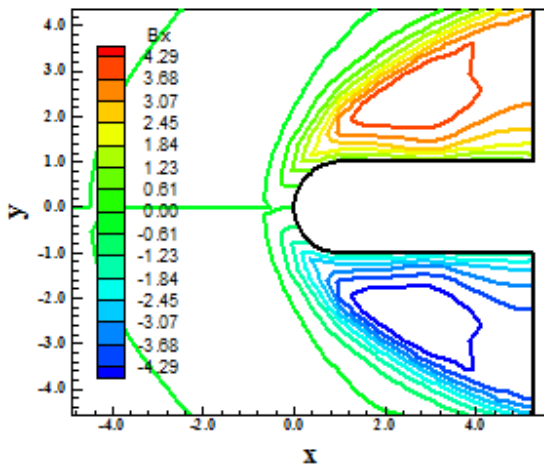

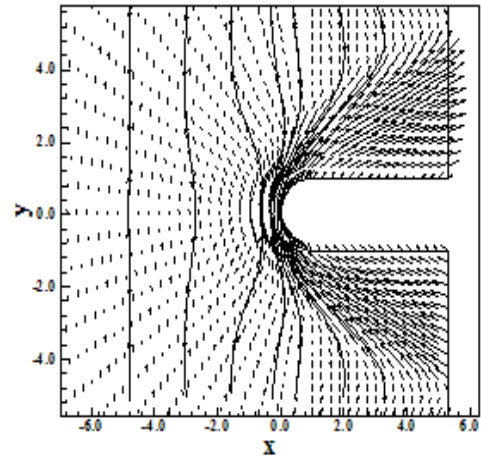Figure 39 : B_x component of magnetic field (JM/A).

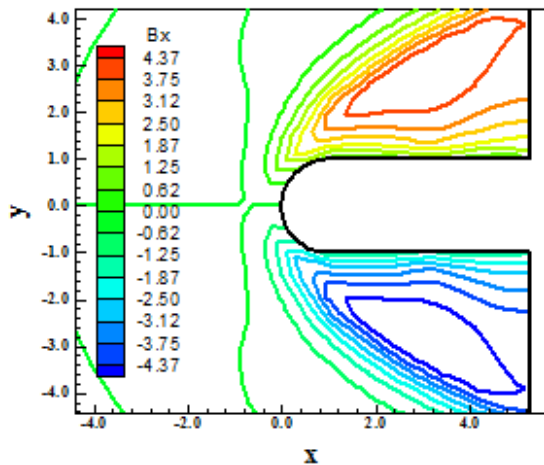Figure 41 : Magnetic field and induction lines (JM/A).

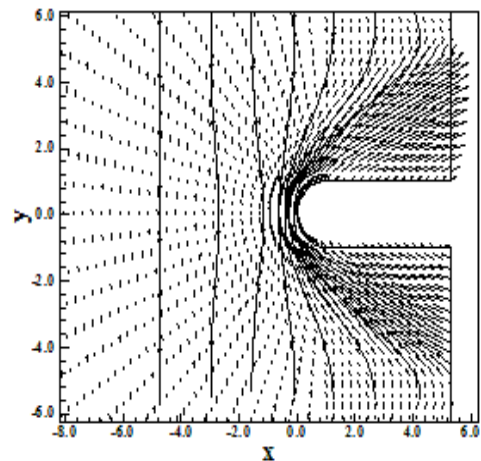Figure 40 : B_x component of magnetic field (JM/M).

Figure 42 : Magnetic field and induction lines (JM/M).

Figures 39 and 40 exhibit the contours of the B_x component of the magnetic field vector determined at the calculation domain. As can be observed, the B_x component is negative at the geometry lower surface and positive at the geometry upper surface, indicating that the magnetic field performs a curve around the geometry, equally observed in the solutions with the [9] scheme. The solutions presented by the [10] scheme with the dissipation models of [12] and of [11] have good symmetry properties. The latter solution presents a B_x field more intense.

Figures 41 and 42 exhibit the magnetic vector field with induction lines to highlight the satisfied initial condition far ahead of the configuration and the distortion in these lines close to the blunt body. As can be observed, the magnetic induction lines are initially attracted to the magnetic field imposed at
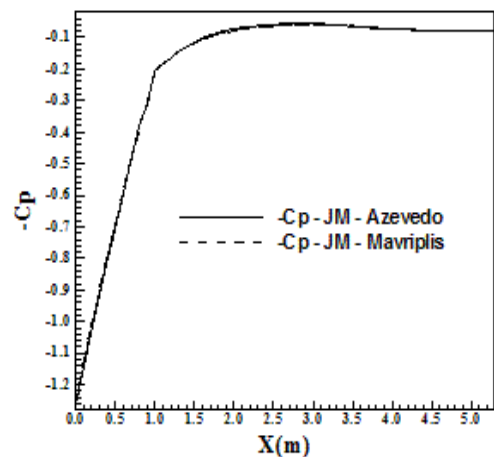

Figure 43 : -Cp distributions.

Figure 43 shows the –Cp distributions along the blunt body wall. As can be seen, the shock captured by the [10] scheme employing both dissipation models present the same intensity. Figure 44 presents the distribution of the translational / rotational temperature along the configuration symmetry line or configuration stagnation line. As can be noted, the dissipation models predict different shock wave positions. The [12] model predicts the shock wave at 1.60m ahead of the blunt body nose, while the [11] model predicts the shock wave at 1.50m ahead of the blunt body nose.
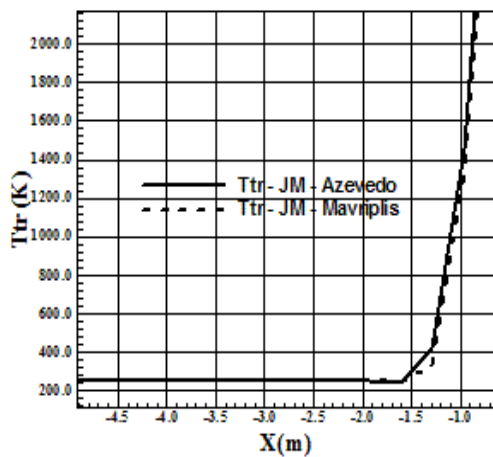

Figure 44 : Shock position by the temperature profile.

7.2.5 Results with the [10] scheme to viscous flow in two-dimensions
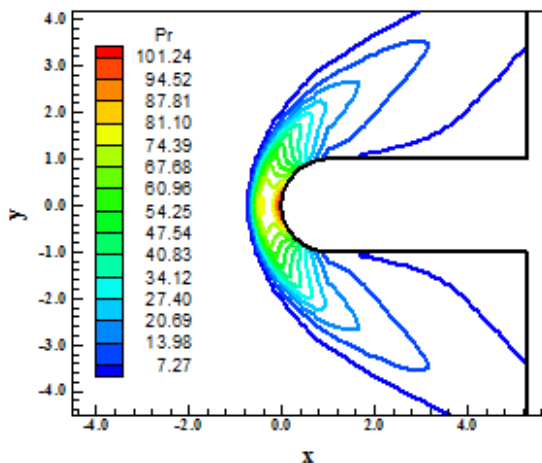

Figure 45 : Pressure contours (JM/A).

Figures 45 and 46 present the pressure contours calculated at the computational domain. The pressure contours obtained by the [10] scheme employing the dissipation model of [12] is more intense than that obtained with the dissipation model of [11], opposed to the behavior observed in the inviscid solution. Good symmetry properties are

observed in both solutions. This field is also more intense than the respective one obtained with the [9] scheme employing the same dissipation model.
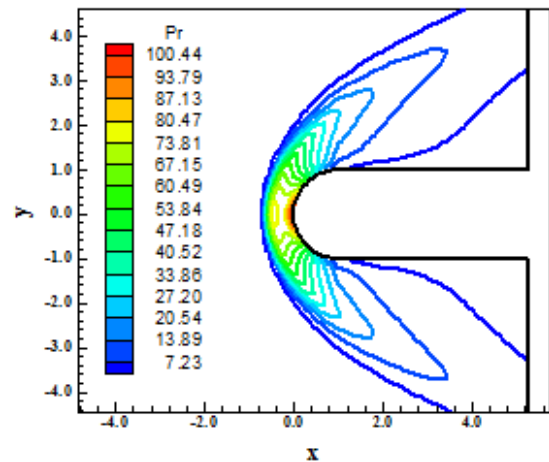

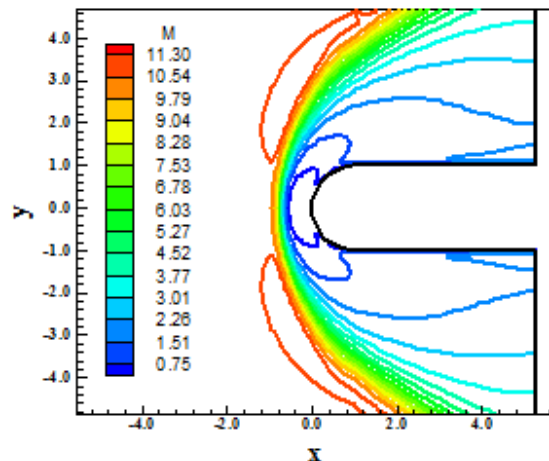Figure 46 : Pressure contours (JM/M).
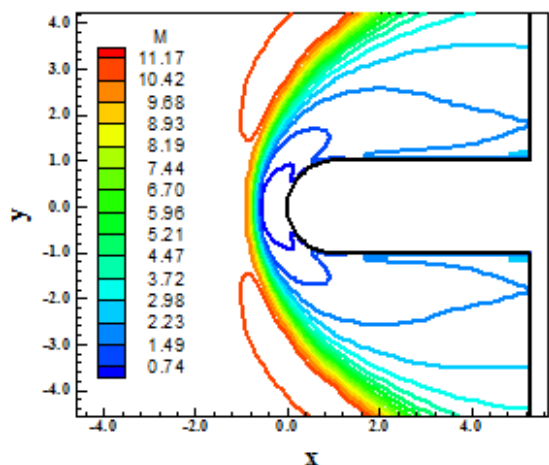

Figure 47 : Mach number contours (JM/A).

Figure 48 : Mach number contours (JM/M).

Figures 47 and 48 exhibit the Mach number contours calculated at the computational domain by

the [10] scheme employing the artificial dissipation models of [12] and of [11], respectively. The Mach number field obtained by the [10] scheme employing the dissipation model of [12] is more intense. It is important to note that both solutions present problems of pre-shock oscillations, being the [11] model solution as more critical. Good symmetry properties are observed in both solutions.

Figures 49 and 50 show the translational / rotational temperature distributions calculated at the computational domain. The [10] scheme with the artificial dissipation model of [12] predicts a more severe temperature field, much more severe than the respective one obtained with the [9] scheme. This field is much more severe than that obtained with the inviscid solution of the present scheme. The temperature peak occurs along the rectilinear walls, by the development of the heating of these by the consideration of viscous effects.
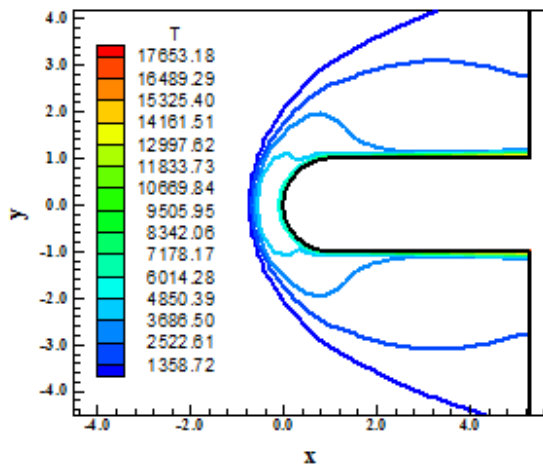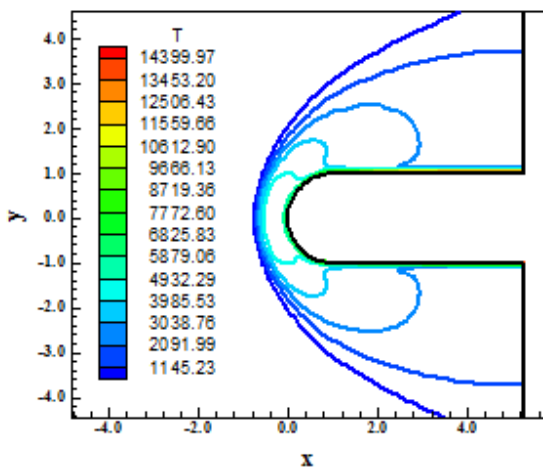

Figure 49 : Temperature contours (JM/A).

Figure 50 : Temperature contours (JM/M).

Figures 51 and 52 exhibit the contours of the B_x component of the magnetic field vector determined

at the calculation domain. As can be observed, the B_x component is negative at the geometry lower surface and positive at the geometry upper surface, indicating that the magnetic field performs a curve around the geometry. The solutions presented by the [10] scheme with the dissipation models of [12] and of [11] have meaningful symmetry properties. The dissipation model of [12] presents a B_x field more intense.
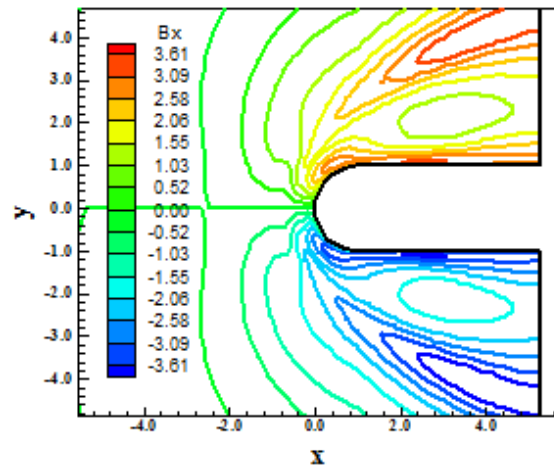
Figure 51 : B_x component of magnetic field (JM/A).
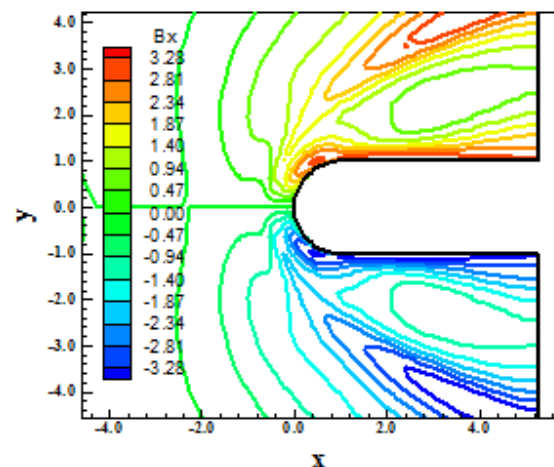
Figure 52 : B_x component of magnetic field (JM/M).

Figures 53 and 54 exhibit the magnetic vector field with induction lines to highlight the satisfied initial condition far ahead of the configuration and the distortion in these lines close to the blunt body. As can be observed, the magnetic induction lines are initially attracted to the magnetic field imposed at the blunt body walls and, close to the body, suffer distortion, getting round the configuration. The same behavior was observed in the respective solutions obtained with the [9] scheme.

Figure 55 shows the –Cp distributions along the blunt body wall. As can be seen, the shock captured

by the [10] scheme employing the [11] dissipation model is more severe than that obtained with the [12] dissipation model, presenting a variation in the Cp value between the nose and the rectilinear walls of the blunt body bigger. Figure 56 presents the distribution of the translational / rotational temperature along the configuration symmetry line or configuration stagnation line. As can be noted, the dissipation models predict the same shock wave positions.
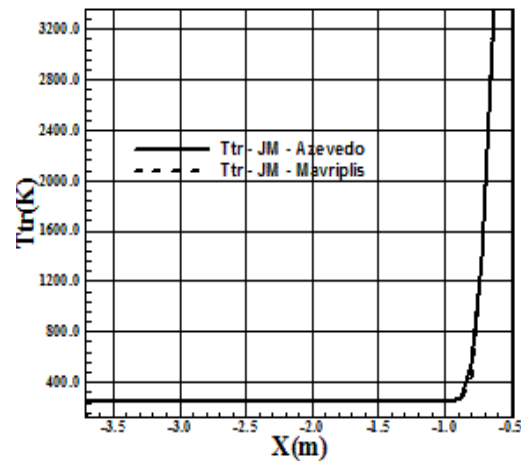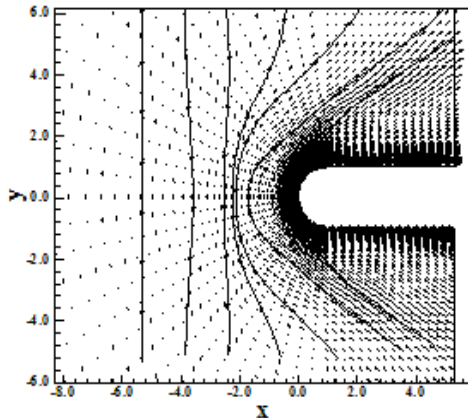

Figure 53 : Magnetic field and induction lines (JM/A).
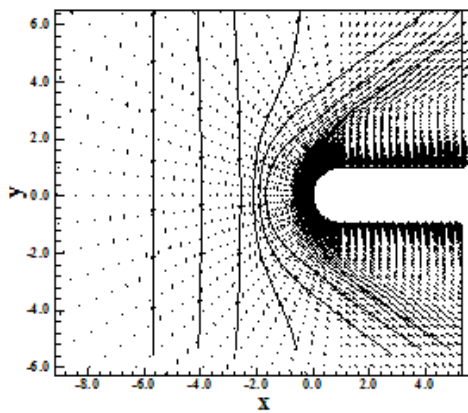
Figure 54 : Magnetic field and induction lines (JM/M).

Figure 55 : -Cp distributions.

Figure 56 : Shock position by the temperature profile.
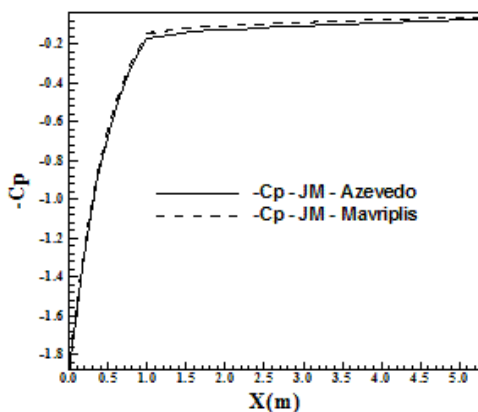
7.2.6 Effects of the shock wave standoff distance with the increase of the magnetic field vector (B_y component) to the inviscid simulations in two-dimensions

To these studies, the [9] and the [10] schemes employing the artificial dissipation operator of [11], which has presented better characteristics of pressure contour severity (-Cp distributions) and shock wave standoff distance than the [12] model, were analyzed. Variations of the $B_{y,\infty}$ component between values from 0.00T (without magnetic field influence) until 0.55T, which has presented a meaningful increase in the shock standoff distance, were simulated.

Figures 57 and 58 exhibit the pressure contours around the blunt body geometry, evaluated at the computational domain, calculated by the [9] scheme with the dissipation model of [11], to the two extreme cases $B_{y,\infty} = 0.00$T and $B_{y,\infty} = 0.55$T. As can be observed, Fig. 57 presents the shock very close to the configuration nose. Figure 58, however, exhibits a shock wave more detached from the configuration nose, which leads to a temperature field less intense, reducing the heating from the configuration nose.

Figure 59 and 60 show the rotational / translational temperature contours around the blunt body geometry, to the two extreme cases $B_{y,\infty} = 0.00$T and $B_{y,\infty} = 0.55$T. As can be observed, the solution without the magnetic field presents a normal shock attached to the configuration nose, while the solution with the maximum value of $B_{y,\infty}$ presents a shock wave more detached from the blunt body nose. Opposed to the expected behavior, the temperature peak in this last solution (with magnetic field different from zero) is bigger than the respective temperature peak of the solution without the influence of the magnetic field, which is

unexpected because with bigger shock standoff distance less the range of reached temperatures. With it, the [9] scheme leads to an error in this evaluation of the temperature field. By this analysis, a heating of the configuration nose when submitted to a magnetic field more intense happened, which is incorrect.

Figure 57 : Pressure contours ($B_{y,\infty} = 0,00T$).

Figure 58 : Pressure contours ($B_{y,\infty} = 0,55T$).

Figure 61 exhibits the pressure along the stagnation line of the blunt body geometry. This distribution serves to define the shock standoff distance along the stagnation line. The graphic is plotted with the non-dimensional pressures along the stagnation line as function of the x coordinate along the symmetry line. As can be observed, as the increase of the $B_{y,\infty}$ intensity is bigger, bigger is the shock standoff distance in relation to the non-influence of the magnetic field. Table 2 exhibits the shock standoff distance to each value of the $B_{y,\infty}$ component. It is possible to conclude from this table that the biggest shock standoff distance occurs to the maximum studied magnetic field, $B_{y,\infty} = 0.55T$,

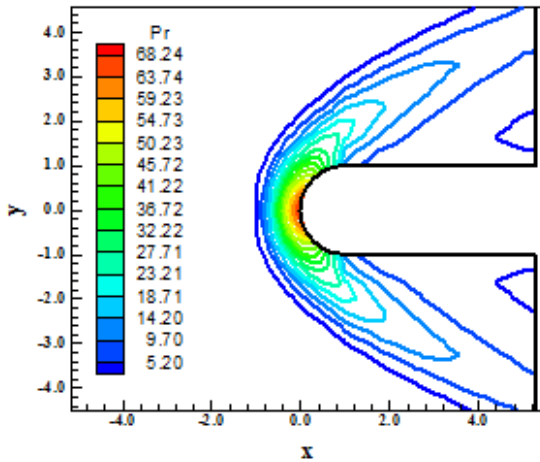corresponding to a distance of 2.40m. These qualitative results accords with the literature: [23]-[24].

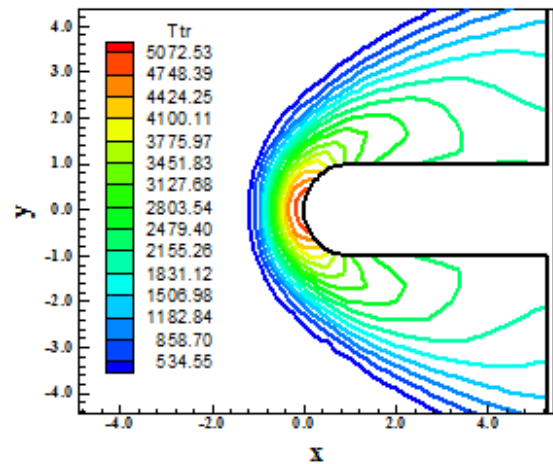Figure 59 : Temperature contours ($B_{y,\infty} = 0,00T$).

Figure 60 : Temperature contours ($B_{y,\infty} = 0,55T$).
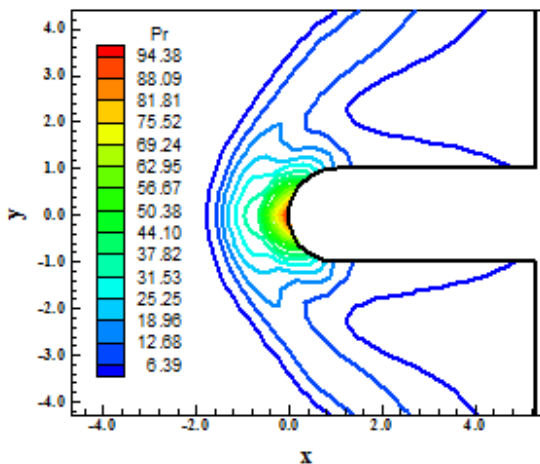

Figure 61 : Pressure distributions at the stagnation line.

Table 2 : Values of normal shock standoff distance due to variations in $B_{y,\infty}$ - [9]

$B_{y,\infty}$ (T)	X_{shock} (m)
0.00	1.50
0.05	1.52
0.15	1.53
0.25	1.59
0.35	1.61
0.45	1.93
0.55	2.40

Figures 62 and 63 exhibit the pressure contours around the blunt body configuration, evaluated at the computational domain, calculated by the [10] scheme with the dissipation model of [11], to the two extreme cases $B_{y,\infty}$ = 0.00T and $B_{y,\infty}$ = 0.55T. As can be observed, Fig. 62 presents the shock attached to the blunt body nose. Figure 63 shows the shock more detached from the configuration nose, which leads to a less intense temperature field, reducing the heating at the nose.
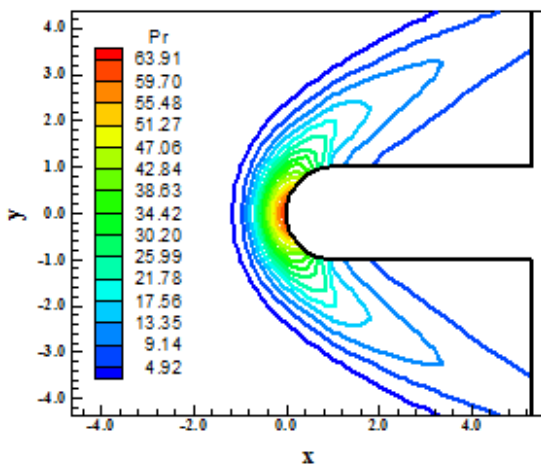
Figure 62 : Pressure contours ($B_{y,\infty}$ = 0.00T).
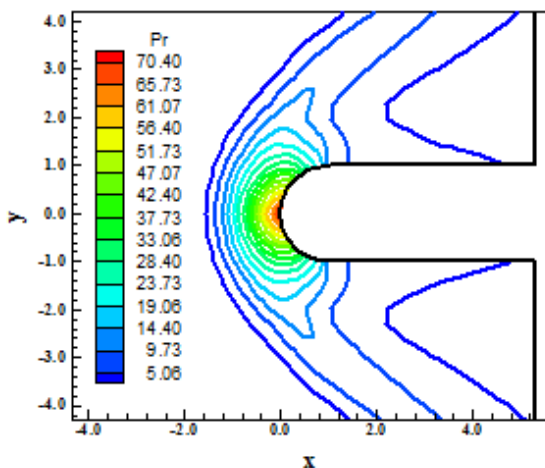
Figure 63 : Pressure contours ($B_{y,\infty}$ = 0.55T).

Figure 64 and 65 present the translational / rotational temperature contours around the blunt body geometry. As can be observed, the solution without the influence of a magnetic field presents a normal shock attached to the configuration nose, while the solution with the maximum value of $B_{y,\infty}$ presents a shock more detached from the blunt body nose. As expected behavior, the temperature peak in the latter solution (with a magnetic field different from zero) is less than the respective temperature peak of the solution without the influence of a magnetic field, which accords with the theory because with bigger shock standoff distance, less the temperature ranges reached by the flow. With it, the [10] scheme presents the correct evaluation of the temperature field. By this analyze, a reduction in the heating of the configuration nose as submitted to a magnetic field more intense is obtained.
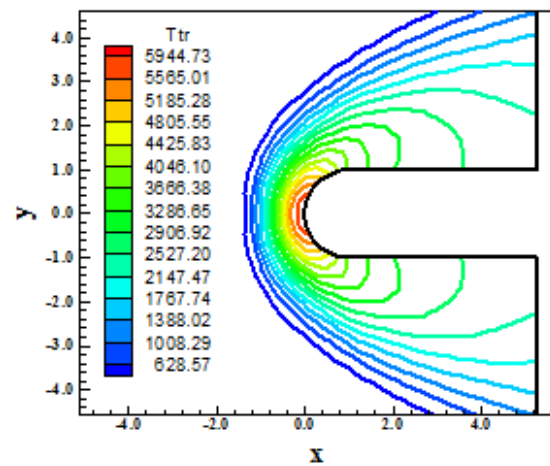
Figure 64 : Temperature contours ($B_{y,\infty}$ = 0.00T).
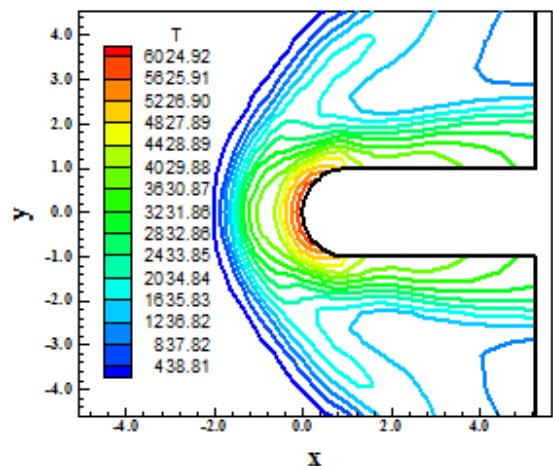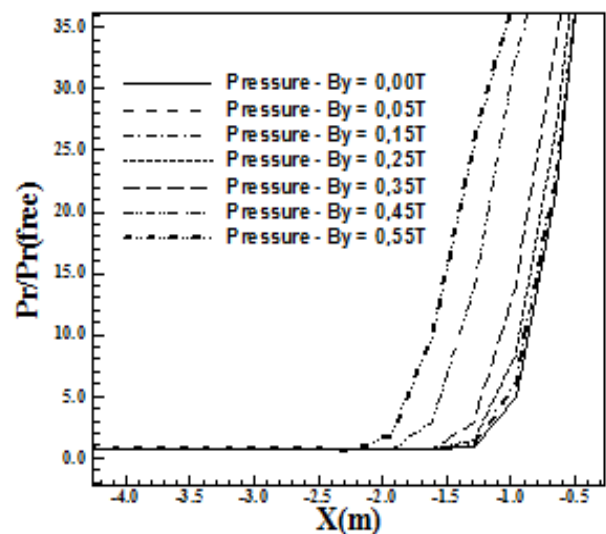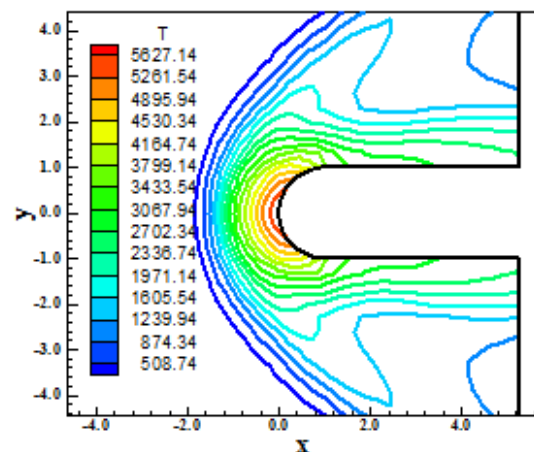

Figure 65 : Temperature contours ($B_{y,\infty}$ = 0.55T).

Figure 66 exhibits the pressure distribution along the stagnation line of the blunt body geometry. This distribution serves to define the shock standoff

distance along the stagnation line. The graphic is plotted with the non-dimensional pressures at the stagnation line as function of the x coordinate along the symmetry line. As can be observed, as the $B_{y,\infty}$ intensity increases, bigger shock standoff distance occurs in relation to the condition of flow without the magnetic field influence. Table 3 presents the shock standoff distance to each value of $B_{y,\infty}$. It is possible to conclude from this table that the biggest normal shock standoff distance occurs to the maximum studied magnetic field of $B_{y,\infty} = 0.55T$, corresponding to a distance of 2.22m. These qualitative results accord to the literature: [23]-[24].

As can be observed, the [10] scheme employing the artificial dissipation model of [11] has presented the solutions more accurate and more consistent, serving as the reference algorithm to this study.
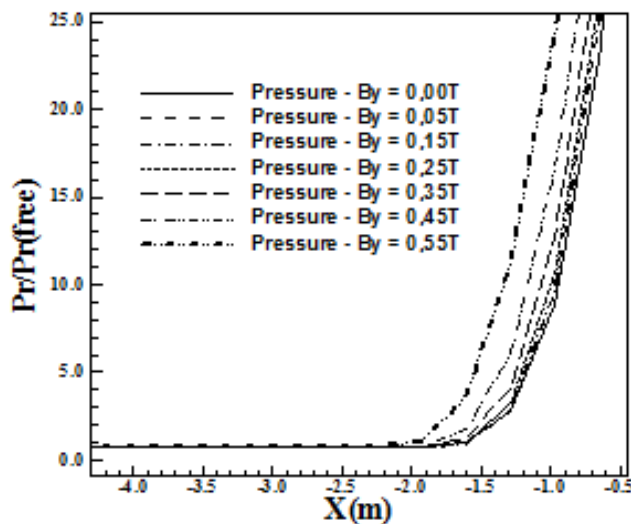

Figure 66 : Pressure distributions at the stagnation line.

Table 3 : Values of the normal shock standoff distance due to variations in $B_{y,\infty}$ - [10].

$B_{y,\infty}$ (T)	X_{shock} (m)
0.00	1.90
0.05	1.88
0.15	1.85
0.25	1.90
0.35	1.91
0.45	2.10
0.55	2.22

7.2.7 Aerodynamic coefficients of lift and drag in two-dimensions

Table 4 presents the aerodynamic coefficients of lift and drag obtained by the blunt body problem, with structured spatial discretization, to a formulation of ideal gas submitted to the influence of a magnetic field in two-dimensions. These coefficients take into account only the consideration of pressure term. The contribution of the friction term was not considered.

Table 4 : Aerodynamic coefficients of lift and drag to the blunt body structured problem submitted to a magnetic field in two-dimensions.

Studied case	c_L	c_D
Inviscid/[9]/[12]	-2.186×10^{-4}	0.343
Viscous/[9]/[12]	1.080×10^{-4}	0.481
Inviscid/[9]/[11]	-3.498×10^{-4}	0.367
Viscous/[9]/[11]	1.602×10^{-4}	0.471
Inviscid/[10]/[12]	1.064×10^{-17}	0.374
Viscous/[10]/[12]	9.262×10^{-17}	0.482
Inviscid/[10]/[11]	4.938×10^{-16}	0.371
Viscous/[10]/[11]	-9.558×10^{-16}	0.475

To the blunt body problem, a symmetrical configuration in relation to the x-axis, a zero value, or close to it, to the lift coefficient is expected. The solution closer to this result is due to the [10] scheme, in inviscid flow, employing the artificial dissipation model of [12]. In general, the solutions with the [10] scheme, with both artificial dissipation models, generate values of c_L much smaller than the respective ones obtained with the [9] scheme. The maximum value of c_D was obtained to the viscous flow, employing the [10] numerical scheme with the artificial dissipation provided by the [12] model.

Table 5 : Comparison between drag aerodynamic coefficients.

Studied case	c_D (without B)	c_D (with B)
Inviscid/[9]/[12]	0.407	0.343
Viscous/[9]/[12]	0.461	0.481
Inviscid/[9]/[11]	0.414	0.367
Viscous/[9]/[11]	0.451	0.471
Inviscid/[10]/[12]	0.458	0.374
Inviscid/[10]/[11]	0.408	0.371
Viscous/[10]/[11]	0.452	0.475

Table 5 presents the drag aerodynamic coefficient calculated without the influence of a magnetic field and with the presence of a magnetic field ($B_{y,\infty} = 0.15T$). As can be observed, in the great majority of the cases, the drag aerodynamic coefficient calculated with the presence of the magnetic field is inferior in value to the same coefficient calculated without the presence of a magnetic field. This behavior is expected and is referred in the CFD literature: [8]. Only in the viscous cases, the drag aerodynamic coefficient

calculated with the presence of a magnetic field is superior to the respective ones calculated without the presence of a magnetic field. As mentioned, this reduction in the value of the drag aerodynamic coefficient, in the inviscid cases, contributes considerable to the minimization of the heating in reentry aerospace vehicles. The [12] model predicts the shock wave at 0.85m ahead of the blunt body nose, opposed to the other observed cases with the [9] scheme and even with the [10] scheme (inviscid case). The shock wave is positioned at 0.85m ahead of the blunt body nose to both dissipation models.

7.3 Computational performance of the studied algorithms

Table 6 presents the computational data of the simulations with magnetic field influence over a blunt body configuration in two-dimensions. The table shows the studied cases, the CFL number of the simulations, the iterations to convergence, the orders of reduction in the magnitude of the maximum residual in the field and the values of k_2 and k_4 employed in each simulation. All cases converged in four (4) orders of reduction of the maximum residual. The distribution of the CFL number was as follows: 0.5 in two cases (25.00%), 0.3 in two cases (25.00%), 0.2 in two cases (25.00%) and 0.1 in two cases (25.00%). The maximum number of iterations to convergence reached less than 18,000 iterations, with the solution of the [9] scheme employing the dissipation model of [11].

Table 6 : Computational data from the simulations with magnetic field acting on a blunt body.

Studied case	CFL	Iterations	Residual Drop	k_2 / k_4
I[(1)]/[9]/[11]	0.3	4,186	4	0.50 / 0.01
V[(2)]/[9]/[11]	0.1	17,975	4	0.75 / 0.01
I/[9]/[12]	0.3	4,434	4	0.50 / 0.01
V/[9]/[12]	0.2	3,760	4	0.50 / 0.01
I/[10]/[11]	0.5	2,945	4	0.25 / 0.01
V/[10]/[11]	0.1	9,962	4	0.50 / 0.01
I/[10]/[12]	0.5	2,400	4	0.25 / 0.01
V/[10]/[12]	0.2	3,797	4	0.25 / 0.01

[(1)]: I = Inviscid; [(2)]: V = Viscous.

In cases in which the [10] scheme was employed, the number of iterations to convergence was inferior to 10,000. The [9] scheme needed to employ the value of 0.75 to the k_2 coefficient (stability in presence of shock waves) in one case to obtain convergence: viscous case with the dissipation model of [11]. The [10] scheme did not need to use the value 0.75 to k_2 coefficient. The maximum k_2 coefficient used by the [10] scheme was 0.50, in the viscous case with the dissipation model of [11]. It is important to emphasize that all viscous simulations were considered laminar, without the introduction of a turbulence model, although a raised Reynolds number was employed in the simulations.

Table 7 : Computational costs of the algorithms in the cases of influence of the magnetic field.

Studied case	Computational cost[(1)]
I/M/A	0.0000087
V/M/A	0.0000230
I/M/Mav	0.0000087
V/M/Mav	0.0000241
I/JM/A	0.0000197
V/JM/A	0.0000580
I/JM/Mav	0.0000202
V/JM/Mav	0.0000569

[(1)] Measured in seconds/per iteration/per computational cell.

Table 7 presents the computational costs of the [9] and of [10] schemes in the formulation which considers the influence of the magnetic field, employing the artificial dissipation models of [11] and of [12]. This cost is evaluated in seconds/per iteration/per computational cell. The costs were calculated employing a notebook with 2.13GHz of clock and 1.0GBytes of RAM, in the Windows Vista Starter environment. The cheapest algorithms were the [9] scheme, in the inviscid simulation, employing both artificial dissipation models, namely [11] and [12], while the most expensive was the [10] scheme, in the viscous simulation, employing the artificial dissipation model of [12]. In relative percentage terms, the former is 566.67% cheaper than the latter. The [10] algorithms are more expensive than the [9] algorithms because the former calculates the flux at interfaces by arithmetical average between the flux vectors, while the latter employ the forward or backward values in relation to the flux interface in each predictor or corrector step, respectively, dismissing the average calculations.

8 Conclusions

The present work aimed to implement a computational tool to simulation of inviscid and viscous flows employing a magnetic field formulation acting on a specific geometry. In this study, the Euler and the Navier-Stokes equations employing a finite volume formulation, following a structured spatial discretization, were solved. The aerospace problem of the hypersonic flow around a blunt body geometry was simulated. A spatially variable time step procedure is employed aiming to accelerate the convergence of the numerical schemes to the steady state solution. Effective gains in terms of convergence acceleration are observed with this technique ([13]-[14]).

The study with magnetic field employed the [9] and the [10] algorithms to perform the numerical experiments. The [10] scheme is calculated by arithmetical average between the convective flux vectors at the flux interface, opposed to the arithmetical average between the conserved variable vector. The viscous flux vectors are calculated by arithmetical average of the conserved variables and of the gradients. This procedure to the viscous simulations is employed by the [9] and by the [10] schemes. The results, mainly those obtained with the [10] algorithm, are of good quality. In particular, it was demonstrated the effect that the imposition of a normal magnetic field in relation to the symmetry line of a blunt body geometry could cause the increase of the shock standoff distance, reducing, hence, the aerodynamic heating. This effect is important and can be explored in the phases of aerospace vehicle project which does reentry in the atmosphere normal to the earth magnetic field. Another option would be the proper vehicle generates an oscillatory electrical field to yield a magnetic field in it and to induce the effect of the increase of the shock standoff distance. These are suggestions to verify.

In relation to the aerodynamic coefficient of lift good values are obtained by the [10] scheme. In relation to the drag aerodynamic coefficients, all the inviscid solutions generated by the magnetic field present values inferior to the respective ones without magnetic field, according to the CFD literature: [8].

The cheapest algorithms were the [9] scheme, in the inviscid simulation, employing both artificial dissipation models, namely [11] and [12], while the most expensive was the [10] scheme, in the viscous simulation, employing the artificial dissipation model of [12]. In relative percentage terms, the former is 566.67% cheaper than the latter. The [10] algorithms are more expensive than the [9] algorithms because the former calculates the

inviscid flux at interfaces by arithmetical average between the flux vectors, while the latter employ the forward or backward values in relation to the flux interface in each predictor or corrector step, respectively, dismissing the average calculations.

9 Acknowledgments

References:

[1] P. A. Davidson, Magnetohydrodynamics in Materials Processing, *Ann. Rev. Fluid Mech.*, Vol. 31, pp. 273-300, 1999.

[2] R. W. Ziemer, W. B. Bush, Magnetic Field Effects on Bow Shock Stand-Off Distance, *Physical Review Letters*, Vol. 1, No. 2, pp. 58-59, 1958.

[3] R. X. Meyer, Magnetohydrodynamics and Aerodynamic Heating, *ARS Journal*, Vol. 29, No. 3, pp. 187-192, 1959.

[4] E. P. Gurijanov, P. T. Harsha, Ajax: New Directions in Hypersonic Technology, *AIAA Paper 96-4609*, 1996.

[5] D. I. Brichkin, A. L. Kuranov, E. G. Sheikin, MHD-Technology for Scramjet Control, *AIAA Paper 98-1642*, 1998.

[6] Y. C. Ganiev, V. P. Gordeev, A. V. Krasilnikov, V. I. Lagutin, V. N. Otmennikov, A. V. Panasenko, Theoretical and Experimental Study of the Possibility of Reducing Aerodynamic Drag by Employing Plasma Injection. *AIAA Paper 99-0603*, 1999.

[7] I. V. Adamovich, V. V. Subramaniam, J. W. Rich, S. O. Macheret, Phenomenological Analysis of Shock-Wave Propagation in Weakly Ionized Plasmas. *AIAA Journal*, Vol. 36, No. 5, pp. 816-822, 1998.

[8] D. V. Gaitonde, Development of a Solver for 3-D Non-Ideal Magnetogasdynamics, *AIAA Paper 99-3610*, 1999.

[9] R. W. MacCormack, The Effect of Viscosity in Hypervelocity Impact Cratering, *AIAA Paper 69-354*, 1969.

[10] Jameson, D. J. Mavriplis, Finite Volume Solution of the Two-Dimensional Euler Equations on a Regular Triangular Mesh. *AIAA Journal*, Vol. 24, No. 4, pp. 611-618, 1986.

[11] D. J. Mavriplis, Accurate Multigrid Solution of the Euler Equations on Unstructutred and

Adaptive Meshes, *AIAA Journal*, Vol. 28, No. 2, pp. 213-221, 1990.

[12] J. L. F. Azevedo, On the Development of Unstructured Grid Finite Volume Solvers for High Speed Flows. *NT-075-ASE-N*, IAE, CTA, São José dos Campos, SP, Brazil, 1992.

[13] E. S. G. Maciel, Analysis of Convergence Acceleration Techniques Used in Unstructured Algorithms in the Solution of Aeronautical Problems – Part I, *Proceedings of the XVIII International Congress of Mechanical Engineering (XVIII COBEM)*. Ouro Preto, MG, Brazil, 2005. [CD-ROM]

[14] E. S. G. Maciel, Analysis of Convergence Acceleration Techniques Used in Unstructured Algorithms in the Solution of Aerospace Problems – Part II, *Proceedings of the XII Brazilian Congress of Thermal Engineering and Sciences (XII ENCIT)*, Belo Horizonte, MG, Brazil, 2008. [CD-ROM]

[15] J. C. Tannehill, D. A. Anderson, R. H. Pletcher, *Computational Fluid Mechanics and Heat Transfer*, Second Edition, Hemisphere Publishing Corporation, 792p, 1997.

[16] E. S. G. Maciel, Comparação entre Diferentes Modelos de Dissipação Artificial Aplicados a um Sistema de Coordenadas Generalizadas – Parte I, *Proceedings of the 7th Symposium of Computational Mechanics (VII SIMMEC)*, Araxá, MG, Brazil, 2006. [CD-ROM]

[17] E. S. G. Maciel, Comparison Among Different Artificial Dissipation Models Applied to a Generalized Coordinate System, *Proceedings of the 8th Symposium of Computational Mechanics (VIII SIMMEC)*, Belo Horizonte, MG, Brazil, 2008. [CD-ROM]

[18] A. Jameson, W. Schmidt, E. Turkel, Numerical Solution for the Euler Equations by Finite Volume Methods Using Runge-Kutta Time Stepping Schemes. *AIAA Paper 81-1259*, 1981.

[19] R. C. Swanson, R. Radespiel, Cell Centered and Cell Vertex Multigrid Schemes for the Navier-Stokes Equations, *AIAA Journal*, Vol. 29, No. 5, pp. 697-703, 1991.

[20] L. N. Long, M. M. S. Khan, H. T. Sharp, Massively Parallel Three-Dimensional Euler / Navier-Stokes Method, *AIAA Journal*, Vol. 29, No. 5, pp. 657-666, 1991.

[21] E. S. G. Maciel, Simulação Numérica de Escoamentos Supersônicos e Hipersônicos Utilizando Técnicas de Dinâmica dos Fluidos Computacional, *Doctoral Thesis*, ITA, São José dos Campos, SP, Brazil, 258p, 2002.

[22] R. W. Fox, A. T. McDonald, *Introdução à Mecânica dos Fluidos*, Editora Guanabara, 632p, 1988.

[23] H-. M. Damevin, J-. F. Dietiker, K. A. Hoffmann, Hypersonic Flow Computations with Magnetic Field, *AIAA Paper 2000-0451*, 2000.

[24] K. A. Hoffmann, H-. M. Damevin, J-. F. Dietiker, Numerical Simulations of Hypersonic Magnetohydrodynamic Flows, *AIAA Paper 2000-2259*, 2000.